UNIVERSIDAD NACIONAL AUTÓNOMA DE MÉXICO
POSGRADO EN CIENCIAS FÍSICAS

ENGINEERING THE SPECTRUM-SPATIAL RESPONSE OF A PHOTON-PAIR SOURCE BASED ON OPTICAL FIBER

TESIS
QUE PARA OPTAR POR EL GRADO DE:
DOCTOR EN CIENCIAS (FÍSICA)

PRESENTA:
DANIEL CRUZ DELGADO

TUTOR
DR. ALFRED U'REN CORTÉS (ICN)

MIEMBROS DEL COMITÉ TUTOR
DR. JOSÉ JIMÉNEZ MIER Y TERÁN (ICN)
DR. JESÚS GARDUÑO MEJÍA (CCADET)

MÉXICO, D. F. MARZO 2018.

CIUDAD DE MÉXICO, MARZO 2018

Abstract

In this work it has been studied two different photon pair sources based on optical fiber through spontaneous four-wave mixing (SFWM) process. The two sources were selected to support several SFWM processes simultaneously, in addition these sources are capable to generate photons which exhibit hybrid entanglement in spectrum-spatial degrees of freedom. In order to characterize the properties of the photon pairs generated, several detection schemes were implemented to measure the spectral behaviour, the transverse mode of propagation and the joint spectral intensity (JSI). Furthermore, confidence theoretical and numerical techniques to describe the SFWM processes in the optical fiber were applied.

Moreover, a mode converter based on optical fiber (mode selective photonic lantern) was used to modify the transverse structure of single photons, which were initially in LP_{01} mode and were generated in optical fiber through SFWM process. The use of the photonic lantern allowed the control over the transverse structure of the photons in such a way that they can be prepared in higher order LP modes, and additionally with explicit orbital angular momentum (OAM). In order to verify the topological charge of the prepared photons, a technique based on far field diffraction was used. The capacity of photonic lanterns to prepare photons in a coherent superposition of several LP modes

suggests that this kind of device can be employed to analyze entangled photon states in transverse structure.

Resumen

En este trabajo han sido estudiadas dos fuentes de parejas de fotones basadas en fibra optica a tráves del proceso de mezcla espontánea de cuatro ondas (SFWM). Las dos fuentes fueron seleccionadas para soportar varios procesos SFWM simultáneamente, además tales fuentes son capaces de generar fotones los cuales exhiben enredamiento híbrido en los grados de libertad espectro-espacial. Para caracterizar las propiedades de las parejas de fotones generados, varios esquemas de detección fueron implementados para medir el comportamiento espectral, el modo transversal de propagación y la intensidad espectral conjunta (JSI). Además, técnicas teóricas y numéricas de confianza fueron aplicadas para describir los procesos SFWM en la fibra óptica.

También, un conversor de modos basado en fibra óptica (linterna fotónica) fue usado para modificar la estructura transversal de fotones individuales, los cuales se encontraban inicialmente en el modo LP_{01} y fueron generados en fibra óptica a través del proceso de SFWM. El uso de la linterna fotónica permitió el control sobre la estructura transversal de los fotones de tal modo que estos pueden ser preparados en modos LP de orden superior, y adicionalmente con momento angular orbital explícito (OAM). Para verificar la carga topológica de los fotones preparados, una técnica basada en difracción de campo lejano fue empleada. La capacidad de las linternas fotónicas para preparar fotones en

una superposición coherente de varios modos LP sugiere que este tipo de dispositivo puede ser empleado para analizar estados de fotones enredados en modo transversal.

Contents

List of Figures

List of Tables

Chapter 1

Introduction

Sources to generate photons with specific properties on polarization, wavelength, transverse mode, purity, etc. are necessary for different purposes such as tests of quantum mechanics [1], quantum communications [2], quantum cryptography [3, 4], quantum key distributions [5, 6], teleportation [7], quantum technologies [8, 9], among others. In order to have the best source possible in each case many devices have been proposed, for instance nonlinear crystals [10], quantum dots [11], optical fibers [12], vapor gases [13], etc.

Some photon sources are based on the interaction of strong electromagnetic fields with optical nonlinear materials, as spontaneous parametric down conversion (SPDC) and spontaneous four-wave mixing (SFWM), where photon pairs are generated. These processes are parametric, i. e., the energy and momentum are conserved and there are no modifications in the nonlinear media. The conservation principles of the two photons generated imply correlations between the photon pair, of spectral, temporal and spatial nature. The photon pair behaviour is described by a Hilbert space, which includes all the degrees of freedom. One way to describe the correlation between the photon pairs is via

Schmidt decomposition, the bipartite system is written in terms of a complete set of basis states. The Schmidt decomposition is described by the parameter K and there are two extreme cases: uncorrelated characterized by a value of $K = 1$ and high correlated with values such that $K \gg 1$. Both cases have particular applications, uncorrelated photons are required for quantum computation [8] and high correlated (entangled) photons are useful for quantum communications and quantum key distribution [5, 6].

The process of SPDC based on optical second-order nonlinearity of some crystals is a very well established way to generate photon pairs [10, 14] that has been exploited over the last years. In SPDC process one pump photon is annihilated inside the nonlinear crystal and two photons are generated, the so-called signal and idler photons. The optical fibers were first used for signal transmission only, and their optical nonlinear properties were eventually used to produce photon pairs via the SFWM process [12]. The SFWM process is based on the optical third-order nonlinearity of the optical fibers, in this process two pump photons of frequencies ω_1 and ω_2 are annihilated inside the fiber and two photons with frequencies ω_s and ω_i are created (signal and idler). The main advantages of SFWM process in optical fiber over SPDC process in crystals to generate photon pairs are: i) the interaction length has no limits, ii) the transverse structure of the generated photons is automatically matched with telecommunications network systems based on fiber optics, and iii) the emission power goes like the square of the pump power, $P_{SFWM} \propto P_{pump}^2$. These characteristics allow a large source brightness and large collection efficiency.

The first kind of optical fiber used consists of two homogeneous elements, core and cladding, the so-called step index profile fiber. But the state of the art for the fiber design makes it possible to fabricate a great variety of fibers that includes step index fibers (SIF), birefringent fibers (BF), photonic crystal fibers (PCF), rare earth doped

fibers, etc. The applications are equally diverse: light amplifiers, telecommunications systems, photon pair generators, supercontinuum generation, etc. Besides, it is possible to apply physical modifications to the fibers like tapering, temperature, stress, etc. to manipulate their dispersive properties. Although the process of SFWM in optical fibers has been well explored in terms of the spectral properties for the generated photon pairs [15, 16, 17] and for the entangled photon pairs [18, 19, 20], the use of transverse higher-order modes has been scarcely studied. The present work tried to explore the spatial, in addition to the spectral properties, over the photon pairs generated. In order to achieve the previous goal, two photon pair sources based on birefringent optical fibers were designed and implemented, where several SFWM processes take place and where the generated photons could have access to transverse higher order modes [21, 22]. These kind of sources are even capable of generate photon pairs with hybrid entanglement.

To control the transverse structure of light many techniques have been used: spatial light modulators [23], phase masks [24], electro-optical schemes [25, 26], among others. The spatial degree of freedom is very promising because specific modes families propagate very well in turbulent media and in the presence of obstacles [27], likewise for applications in the light-matter interactions [28], also for data transmission applications [29], etc. In this work will be described a technique to manipulate the transverse structure of single photons using a fiber based device: a mode selective photonic lantern (MSPL) [30]. Due to the fiber based nature of the source and the mode converter, it could be possible to translate the entire experimental setup to one all-in-fiber device.

A mode selective photonic lantern is a passive fiber device where the light can transits from a fundamental mode towards a higher order mode, the light is launched in a single mode fiber and finished in a multi mode fiber [31, 32]. In addition, photonic lantern device allows orbital angular momentum generation, and it is directly matching with

optical fiber telecommunications networks.

1.1 Objectives

The present work has the objective of design and implement a photon pair source via spontaneous four-wave mixing process employing birefringent optical fibers as nonlinear media, in such a way that specific properties of the generated photons will be obtained (spectral correlations, spectral tuning, access to several transverse modes). In addition a detailed description of the process is required, to model the medium dispersion, the generation condition, and the two photon state. The particular objectives of the work are:

- To mount a specific photon pair source based in birefringent optical fiber.
- To make the characterization of the generated photon pair (spectral behaviour, transverse mode and joint spectral intensity).
- To describe the spontaneous four-wave mixing process in the source, apply mathematical and numerical tools for fiber dispersion, model the generation condition, and describe the two photon state of the generated photons.
- To control the transverse spatial properties of the single photons using a mode selective photonic lantern.

1.2 Thesis Outline

The work is divided in 7 chapters including the introduction. The Chapter 2 contains the basis about optical fibers, a discussion about the fiber properties, the description of the

light guided in fibers. The Chapter 3 describes the spontaneous four wave mixing process and how to characterize the generated photons. The Chapter 4 includes the mode selective photonic lantern operation principle. The Chapter 5 includes the experimental results of the spontaneous four wave mixing processes in optical fiber, the preparation of the source and the detection schemes. The Chapter 6 discusses the manipulation of single photons with the photonic lantern. Finally, the Chapter 7 includes the main conclusions of the work.

Chapter 2

Properties of Optical Fibers

When an electromagnetic field interacts with matter a number of possibilities can occur, ranging from classical phenomena to quantum processes. The nature of processes depends of the light as well as the medium. Along the next lines only a brief introduction to the theory will be shown. First, the classical description of the processes of light in optical fibers and then the quantum description for the photon pair generation through the spontaneous four-wave mixing process.

2.1 Principles on Optical Fibers

An optical fiber is a waveguide with cylindrical geometry. The simplest type is the step index fiber which consists of a core surrounded by a cladding, the refractive index is constant in each part. The refractive index values are such that $n_{core} > n_{cladding} > n_{air}$, as is shown in figure 2.1a). The basic principle behind the operation of the optical fiber is the total internal reflection: considering two media with refractive index n_2 and n_1 respectively and such that $n_1 > n_2$, the light traveling from the medium with n_1 towards

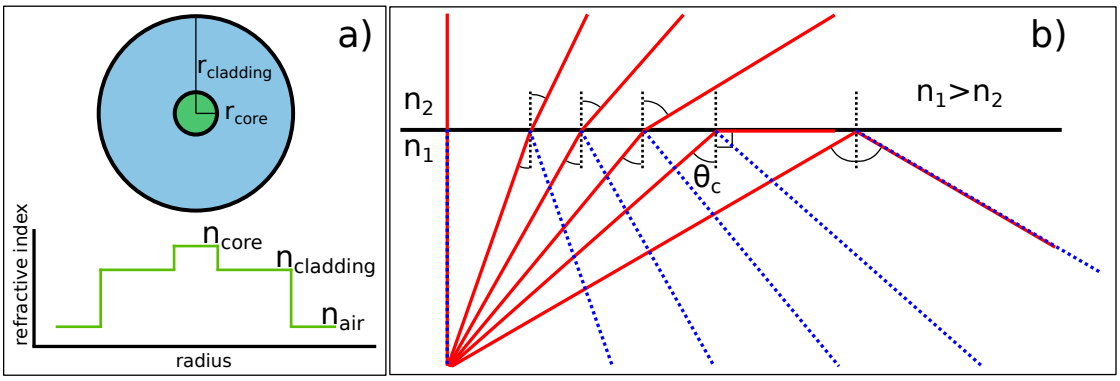

Figure 2.1: a) Step index fiber profile. b) Total internal reflection principle.

the medium with n_2 will be refracted following the Snell law $n_1 \sin(\theta_1) = n_2 \sin(\theta_2)$. If the light incides at an angle larger than a specific value $\theta_c = \sin^{-1}(n_2/n_1)$ it will be totally reflected, see figure 2.1b). This value defines the so-called critical angle.

The optical fibers are usually made of fused silica and doped with other materials to raise or to lower the refractive index in terms of the particular needs. The flexibility in fiber design and manufacturing allows to access a really great variety of fibers: step index, graded index, photonic crystal fiber, erbium doped, among others. This variety makes it possible to apply optical fibers in many fields: telecommunications, sensing, lasers, quantum optics, etc.

There are some parameters that characterize the optical fibers: numerical aperture, dispersion, V parameter, mode field diameter, among others. Only the relevant parameters for the present discussion will be presented. The numerical aperture (NA) of a fiber is on the one hand related to the range of angles where the light can enter or emerge from the fiber, and on the other hand it is also related with the refractive indices of the fiber. The NA is written as

$$NA = n_{medium} \sin(\theta_{max}) = \sqrt{n_{core}^2 - n_{cladding}^2}, \tag{2.1}$$

where n_{medium} corresponds to the refractive index of the medium from where the light comes or goes, like air, and n_{core} and $n_{cladding}$ are the core and cladding refractive indices of the fiber.

There are different contributions to dispersion process: chromatic, birefringent, modal, etc. Chromatic dispersion is one of the most important effects in light propagation in optical fibers, accordingly, it will be discussed in a separate section.

2.2 Chromatic Dispersion

The response of the dielectric medium to an electromagnetic field depends of the frequency ω. This characteristic of the medium can be seen in the refractive index dependence $n(\omega)$, which can be described through the Sellmeier equation far from the medium resonances [33] as

$$n^2(\omega) = 1 + \sum_j \frac{\zeta_j^2 \omega_j^2}{\omega_j^2 - \omega^2}, \tag{2.2}$$

where ω_j is the j resonance frequency and ζ_j is the strength of the jth contribution. In practice is enough to consider until the third term in the sum, the coefficient values as appear in 2.2 for fused silica are $\zeta_1 = 0.6961663$, $\zeta_2 = 0.4079426$, $\zeta_3 = 0.8974794$, $\lambda_1 = 0.0684043\mu m$, $\lambda_2 = 0.1162414\mu m$, $\lambda_3 = 9.896161\mu m$.

From the dispersion relation it is possible to see that the wavenumber is a function of the frequency. The wavenumber can be written in terms of the refractive index as $k = (n(\omega)\ \omega)/c$. Expanding the wavenumber k in a Taylor series around ω_0 at which

the pulse spectrum is centered

$$k(\omega) = k_0 + k_1(\omega - \omega_0) + \frac{1}{2}k_2(\omega - \omega_0)^2 + \ldots, \tag{2.3}$$

where $k_m = d^m k/d\omega^m|_{\omega=\omega_0}$. The second term is related to the group velocity, $k_1 = 1/v_g$, while the third term is related to the group-velocity dispersion (GVD). The group velocity is the velocity at which the envelope of an optical pulse moves, and the group-velocity dispersion is related to the pulse broadening. In order to illustrate the wavelength dependence of the terms, in figure 2.2 is shown the behaviour of the wave number and refractive index as a function of the wavelength for a fiber with $r = 1.6\mu m$ and $NA = 0.27$ values

The wavelength λ_D at which $k_2 = 0$ is called zero-dispersion wavelength. Sometimes is common to use the parameter $D = -2\pi c k_2/\lambda^2$ instead of k_2. The parameter D is a measure of the pulse spreading per unit bandwidth per unit length of the medium of transmission. The region of wavelengths such that $\lambda < \lambda_D$ implies $D < 0$ and is called the normal dispersion region, meanwhile the region of wavelengths where $\lambda > \lambda_D$ implies $D > 0$ is called the anomalous dispersion region. The dispersion behaviour is quite different depending of the region where it takes place. Among the capacities to design and manufacture optical fibers it is possible to tune the zero-dispersion wavelength.

2.3 Fiber Nonlinearities

The interaction between an electromagnetic field and a dielectric medium causes a redistribution of the charge in each atom or molecule, causing a polarization. The macroscopic response can be described in terms of the electric polarization and can be modeled as a power series of the electric field

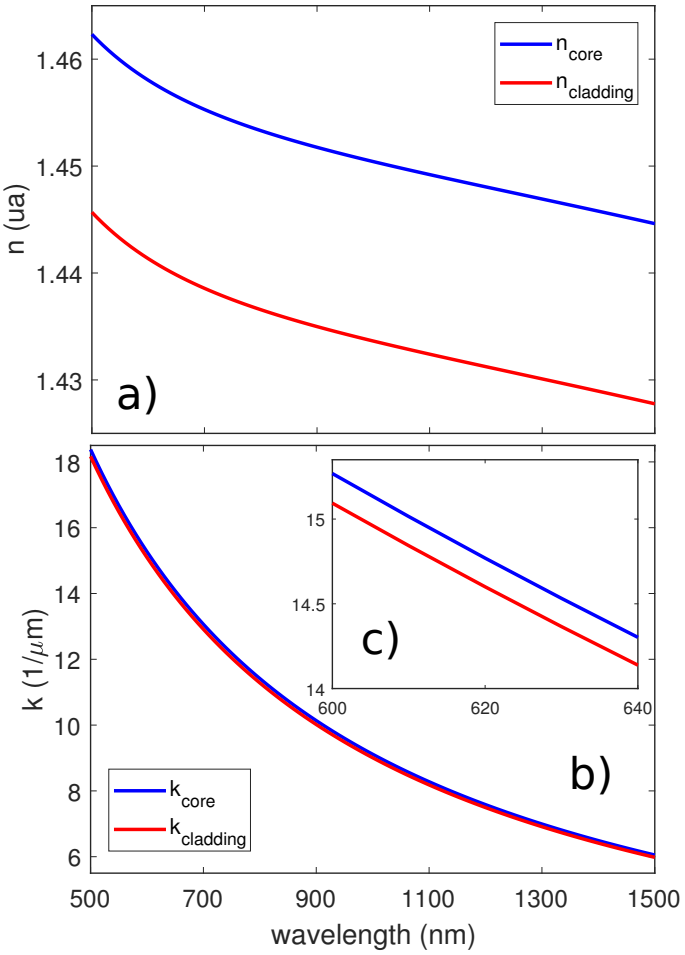

Figure 2.2: a) Refractive index and b) wave number as a function of wavelength. c) Zoom of the wave number.

$$P_i = \epsilon_0[\chi_{ij}^{(1)} E_j + \chi_{ijk}^{(2)} E_j E_k + \chi_{ijkl}^{(3)} E_j E_k E_l + \ldots], \tag{2.4}$$

where ϵ_0 is the vacuum electric permittivity and $\chi^{(q)}$ corresponds to the electric susceptibility of order q, this susceptibility is a $q+1$ rank tensor. The subindices i, j, k and l represent the vector components, the summation convention of repeated indices has been assumed. In equation (2.4) an instantaneous response of the medium has been assumed, which corresponds to a lossless medium. The equation (2.4) is appropriate for a non-dispersive medium, or under circumstances when the effective frequencies of the field are not too close to the resonance frequencies of the medium. The material effects due to higher terms of the polarization $q > 1$ are nonlinear in nature. The structural characteristics and the medium's geometry determine the nonlinear responses. Optical fibers are made of fused silica (SiO_2), this is a centrosymmetric material and, therefore, does not produce second order optical nonlinearities. The smallest optical nonlinear effects are due to the third order susceptibility $\chi^{(3)}$, this term is responsible for processes where four waves are involved as third harmonic generation, four-wave mixing, etc.

2.3.1 Nonlinear Refraction

As it has been mentioned, in optical fibers the nonlinear effects of lowest order come from the third order susceptibility $\chi^{(3)}$, this term leads to the intensity dependence of the refractive index [33], which can be written as

$$n(\omega, |E|^2) = n_0(\omega) + n_2|E|^2, \tag{2.5}$$

where $n_0(\omega)$ is the refractive index given by equation (2.2), $|E|^2$ is the optical intensity within the fiber and n_2 is the nonlinear refractive index given by

$$n_2 = \frac{3}{8n_0} Re(\chi^{(3)}_{xxxx}), \tag{2.6}$$

where Re represent the real part, the optical field is assumed to be linearly polarized so that only one component $\chi^{(3)}_{xxxx}$ of the fourth-rank tensor contributes to the refractive index.

The intensity dependence of the refractive index leads to a large number of interesting nonlinear effects, two of the most widely studied ones are self-phase modulation (SPM) and cross-phase modulation (XPM). Self-phase modulation refers to the self-induced phase shift experienced by an optical field during its propagation. Cross-phase modulation refers to the nonlinear phase shift of an optical field induced by another field with a different wavelength, direction of propagation, or polarization.

2.3.2 Non Parametric Processes

In addition to the energy conserved processes related with the third order susceptibility $\chi^{(3)}$, inelastic processes are also possible in the fiber, such as Raman scattering (RS) and Brillouin scattering (BS). Both processes are related to the vibrational excitation modes of silica [33], and the main difference between them is that optical phonons participate in RS while acoustic phonons participate in BS.

In Raman and Brillouin scattering processes Stokes and anti-Stokes photons are produced, the Stokes generation occurs when one pump photon excites one phonon and loses energy $\nu_{photon} = \nu_{phonon} + \nu_{Stokes}$, and the second occurs when one pump photon absorbs one phonon and gains energy $\nu_{photon} + \nu_{phonon} = \nu_{anti-Stokes}$. The anti-Stokes photons are generated with lower probability than Stokes ones because to generate them it is indispensable that the material be in a particular state a priori. In figure 2.3 the

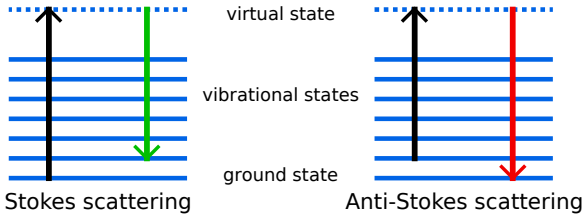

Figure 2.3: Stokes and anti-Stokes energy diagram.

energy diagram of Stokes and anti-Stokes generation is shown.

In silica, the main Raman scattering peak can be observed at a frequency detuning of approximately $13THz$ with respect to the incoming frequency. In addition, the production rate of photons from Raman scattering process is a linear function of the pump power. Photons produced by non parametric processes can degrade the correlations of the photon pairs produced by parametric process, as those produced by spontaneous four-wave mixing, it is a reason to try to avoid them. Due to the vibrational origin of the Raman photons, a possible solution to decrease their production rate is cooling the optical fiber.

2.4 Guided Waves

An step-index optical fiber, see figure 2.1a), is a waveguide that confines the electromagnetic field propagation. The modes of propagation are called guided waves or guided modes, these modes are the spatial distributions of the electromagnetic field intensity traveling along the axis of the fiber. The fibers where only the fundamental mode is allowed to propagate are referred as single-mode. The properties of the modes of propagation are obtained as a solution to the Maxwell's equation subject to the boundary conditions imposed by the fiber [34]. Both field vectors, the electric $\overline{E}$ and the magnetic

$\overline{H}$ obey the wave equation. An harmonic field is assumed, also cylindrical geometry and propagation along the z axis is considered, then it is possible to propose a solution as

$$\overline{A}(\overline{r},t) = \overline{A}(r,\phi)\exp\left(i(\omega t - \beta z)\right), \tag{2.7}$$

where r and ϕ are the polar coordinates and β is the z component of the wave vector also known as the propagation constant, still to be determined. The exact solution to equation (2.7) implies to solve the wave equation in cylindrical coordinates, and the exact solutions are complicated in general because the six components of the electromagnetic field are different of zero [34]. The confined modes exist if fulfill the condition $k_0\, n_{core} > \beta > k_0\, n_{cladding}$, this condition is obtained from the wave equation and because the field amplitudes are zero at infinity.

When the index difference is small enough $n_{core} - n_{cladding} << 1$, this leads to a tremendous simplification in matching the field components at the core-clad interface, then it is possible to solve the wave equation in Cartesian components. The solutions for the E field of a y polarized solution is given by

$$\begin{aligned} E_x &= 0, \\ E_y &= \begin{cases} AJ_l(hr)e^{il\phi}\exp i(\omega t - \beta z),\ r < r_{core}, \\ BK_l(qr)e^{il\phi}\exp i(\omega t - \beta z),\ r > r_{core}, \end{cases} \end{aligned} \tag{2.8}$$

where A and B are constants, $h = \sqrt{n_{core}^2 k_0^2 - \beta^2}$ and $q = \sqrt{\beta^2 - n_{cladding}^2 k_0^2}$, J_l and K_l are Bessel functions. All the other field components can be obtained from the expressions in equation (2.8) using the Maxwell's equations. The constant B takes the form $B = AJ_l(hr_{core})/K_l(qr_{core})$ to ensure the continuity of E_y at the core-cladding boundary. Finally, the constant A is determined by the normalization condition. The solutions

for the E field of a x polarized solution is totally analogous to the previous description in equation (2.8) for the y polarized solution. Based on the circular symmetry of the fiber, the two polarization solutions of the guided modes have the same propagation constant and the same intensity and power distribution [34]. Using the electromagnetic field expressions it is possible to derive the mode condition

$$hr_{core}\frac{J_{l+1}(hr_{core})}{J_l(hr_{core})} = qr_{core}\frac{K_{l+1}(qr_{core})}{K_l(qr_{core})}. \tag{2.9}$$

The eigenvalues obtained from equation (2.9) are labeled β_{lm}, with $l = 0, 1, 2, \ldots$ and $m = 1, 2, 3, \ldots$ The labels l and m are related to the number of maxima of the spatial profile along the azimuthal and radial directions, respectively. This mode basis is called linearly polarized LP_{lm} (LP). The mode index l is related to the orbital angular momentum (OAM) of light. A mode with subindex l corresponds to a linear combination of contributions with azimuthal dependence $exp(\pm il\phi)$, i.e., with topological charge $\pm l$. In figure 2.4 the intensity profile of the transverse modes in LP_{lm} basis is shown.

For a step index fiber with the index difference condition, at a given frequency ω, the number of guided modes is determined by the V parameter, which can be written as

$$V = k_0\, r_{core}\, (n_{core}^2 - n_{cladding}^2)^{1/2} = \sqrt{(hr_{core})^2 + (qr_{core})^2}, \tag{2.10}$$

where $k_0 = 2\pi/\lambda$ is the wave number. Using the mode condition given in equation (2.9) and the expression for the V parameter it is possible to derive that if $V < 2.405$ the fiber only supports the fundamental mode, while for $V > 2.405$ the fiber supports more than one mode.

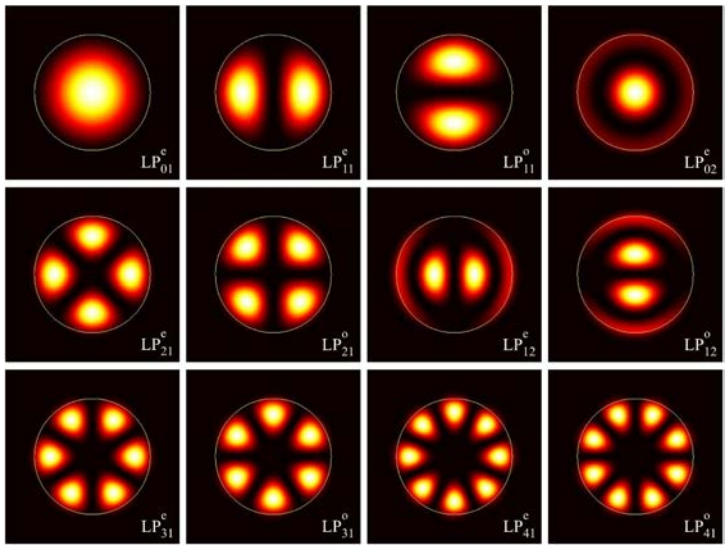

Figure 2.4: Intensity profile of the transverse modes in LP basis.

Modal Dispersion It is important to note that modes with different β_{lm} values travel at different velocities in the optical fiber, this effect is know as modal dispersion.

2.5 Birefringent Optical Fibers

As it has been mentioned in the previous section, the fundamental mode that propagates in a single-mode fiber is actually a degenerate combination of two orthogonally-polarized modes. In practice the light can transfer from one of these modes to the other if any sort of perturbation affects the fiber, either intrinsic or extrinsic.

Among the different types of optical fibers there is a specific kind known as polarization maintaining (PM) or birefringent fiber with the property that it preserves the polarization of the incident light, even under external disturbances. The technique to preserve the polarization in PM fibers consists of breaking the symmetry of the fiber applying transversal stress in the fiber, inducing a birefringence in the fiber. In PM

fibers the two orthogonally-polarized modes are forced to travel at different velocities, i.e. with different propagation constants. This velocity difference is an obstacle for light to couple from one polarization to another, as a result, the polarization of incident light is preserved along the fiber while it propagates. In order to obtain two different propagation velocities in the fiber, an anisotropy in the refractive index is produced in the core, this anisotropy is obtained through the application of controlled uniaxial stress or by modifying the geometry. Several schemes to obtain the birefringence in optical fibers are shown in figure 2.5. To obtain the uniaxial stress in PM optical fibers is common the use of stress bars, see figure 2.5a) and figure 2.5b). The stress bars define two main axes, the slow axis is parallel to stress agents while the fast axis is orthogonal to stress agents see figure 2.5e).

In order to describe the capability of PM fibers to preserve the polarization, it is common to use the beat length. The light travels at different velocities when it propagates along the two axes, the light coupled and traveling through the fiber will interfere at regular intervals along the fiber, this is the beat length. Bright and dark fringes regions will appear separated by the beat length which can be written as

$$L_P = \frac{\lambda}{B}, \tag{2.11}$$

where λ is the wavelength of the traveling light, and $B = n_{slow} - n_{fast}$ is the birefringence, see figure 2.6.

Polarization Dispersion The difference in the propagation constant, for the two modes with orthogonal polarizations, is referred to as modal birefringence, the strength of this modal birefringence can be defined as

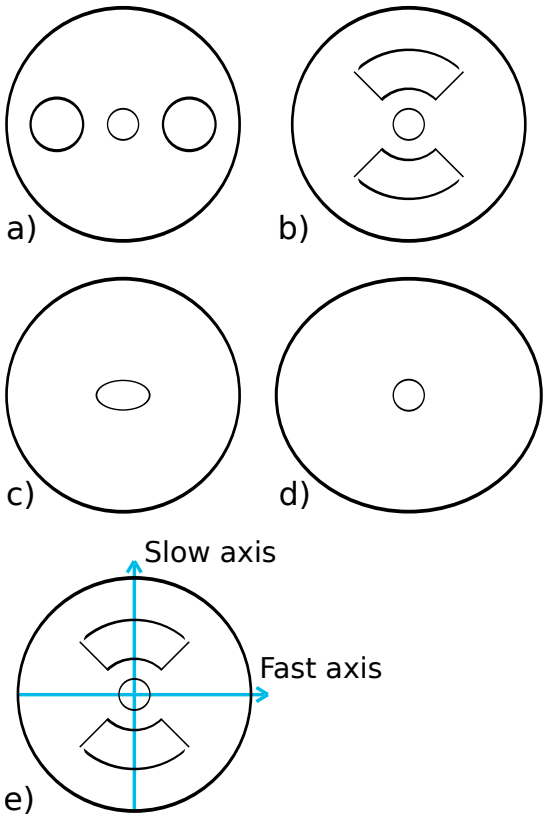

Figure 2.5: Profiles of birefringent fibers, a) Panda, b) Bowtie, c) Elliptical core, d) Elliptical cladding, and e) Axis defined by the stress bars.

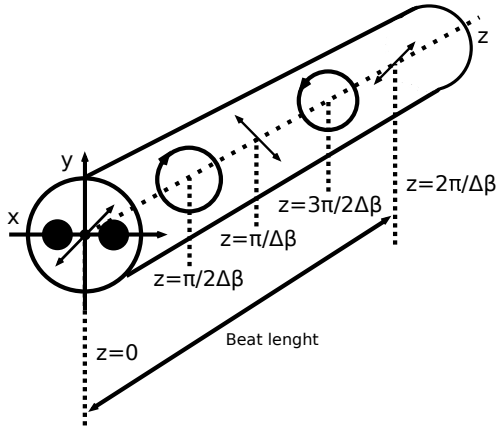

Figure 2.6: Beat length in terms of the propagation constant.

$$k_m = \frac{|k_x - k_y|}{k_0} = |n_x - n_y|, \tag{2.12}$$

where n_x and n_y are the modal refractive indices for the x and y polarizations respectively.

2.5.1 Modified Step Index Model 1

In order to model the dispersion of a step index fiber it is necessary to consider the core size and the numerical aperture. While for fibers with complicated profiles as the birefringent ones, the step index fiber is the starting point, then a suitable modification is made. For a PM fiber with stress bars in one axis, see figure 2.5, the dispersion of the two principal axes is considered equal given by the refractive index $n_0(\omega)$, then a constant offset Δ is added to the refractive index that corresponds to the slow axis as

$$n(\omega) = \begin{cases} n_{slow}(\omega) = n^0_{lm}(\omega) + \Delta, \\ n_{fast}(\omega) = n^0_{lm}(\omega), \end{cases} \tag{2.13}$$

where n^0_{lm} is the refractive index for transverse mode LP_{lm} only. In this way it is possible to express the propagation constant $\beta_{lm,\mu}$ for both axes $\mu = slow, fast$ of the fiber and for any transverse mode LP_{lm}.

2.5.2 Modified Step Index Model 2

The model described by equation (2.13) is the usual way to describe birefringent fibers [16]. Nevertheless, it is feasible to improve that basic model. An additional modification to the previous description consists of considering a parity birefringence [37], this modification is necessary in order to take into account the symmetry breaking caused

by the stress agents in the fiber.

For circularly symmetric fibers the azimuthal dependence of the LP modes can be expressed in terms of two different bases { $\exp(il\phi)$, $\exp(-il\phi)$ } or { $\sin(l\phi)$, $\cos(l\phi)$ }. However, when the azimuthal symmetry is broken which is the case for birefringent optical fibers, modes have a well-defined even or odd parity and modes with an exponential $\exp(\pm il\phi)$ azimuthal dependence are in fact not supported. Thus, for a birefringent optical fiber the propagation modes are correctly expressed in the { $\sin(l\phi)$, $\cos(l\phi)$ } basis, with an appropriate parity-dependent propagation constant.

Besides the number of radial and azimuthal maxima, each propagation constant has two additional parameters: polarization p and parity q. In this way each propagation constant is identified as β_{lm}^{pq} for both axes $p = slow, fast$, for both parities $q = e, o$, and for any transverse mode LP_{lm}. For example considering the LP_{01} mode, it actually includes two modes with the same intensity profile but with orthogonal polarizations. Something similar happens with the LP_{11} mode, it includes four modes with different combinations of intensity profile and polarizations. In general all modes LP_{lm} such that $l \geq 1$ will unfold into four separate modes, which become nondegenerate in fibers that depart from circular symmetry. The nondegenerate LP_{01} and LP_{11} modes are illustrated in figure 2.7

The way to describe the unfolded refractive index caused by the parity breaking is adding an additional offset Δ_p in the refractive index corresponding to the odd parity mode as

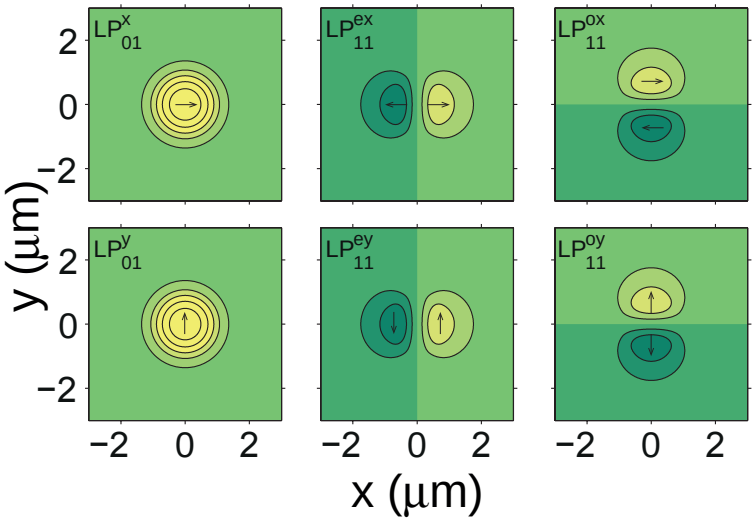

Figure 2.7: Unfolded LP modes in parity and polarization terms.

$$n(\omega) = \begin{cases} n_{o,slow}(\omega) = n^0_{lm}(\omega) + \Delta + \Delta_p, \\ n_{o,fast}(\omega) = n^0_{lm}(\omega) + \Delta_p, \\ n_{e,slow}(\omega) = n^0_{lm}(\omega) + \Delta, \\ n_{e,fast}(\omega) = n^0_{lm}(\omega), \end{cases} \tag{2.14}$$

where n^0_{lm} is the refractive index for transverse mode LP_{lm}.

Chapter 3

Spontaneous Four-Wave Mixing

Spontaneous Four-Wave Mixing (SFWM) is a third order nonlinear process which can take place in optical fibers. The SFWM is a parametric process, no energy is lost or gained in the medium. There are four optical waves involved, two photons of frequencies ω_1 and ω_2 are spontaneously annihilated inside the fiber and two photons of frequencies ω_s and ω_i are created, those last referred as signal and idler respectively. The energy and momentum conservation condition are summarized in the phasematching condition

$$\Delta k_j = \beta(\omega_1, \alpha_j) + \beta(\omega_2, \beta_j) - \beta(\omega_s, \mu_j) - \beta(\omega_1 + \omega_2 - \omega_s, \nu_j) - \phi_{NLj} = 0, \qquad (3.1)$$

where $\omega_i = \omega_1 + \omega_2 - \omega_s$ has been assumed as part of the energy conservation, a propagation constant β for each wave involved is considered, these propagation constants are functions of the frequency ω ($\omega = \omega_1, \omega_2, \omega_s, \omega_i$) and the transverse mode ξ ($\xi = \alpha_j, \beta_j, \mu_j, \nu_j$). In addition, a nonlinear term is included due to self- and cross-phase modulation effects. The equation (3.1) is labeled with a j index to indicate a partic-

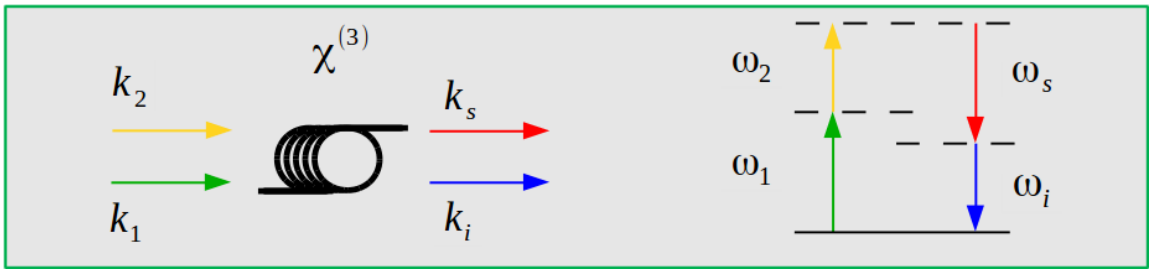

Figure 3.1: SFWM energy and momentum diagram.

ular process. The phasematched processes $\Delta k_j = 0$ dominate over non phasematched processes in terms of conversion efficiency. In phasematching equation (3.1) has been assumed a configuration where the four waves (the two pumps and the generated photons) travel in the same direction, i.e. they co-propagate. In figure 3.1 the energy momentum diagram is shown, each of the four waves involved in the third order nonlinear process is characterized by ω and β values, and all are traveling in the same direction.

Besides the direction of propagation, several combinations of polarization are possible in the SFWM process:

i) The four waves have the same polarization, these processes are related to the χ_{xxxx} (or χ_{yyyy}) element of the third order susceptibility tensor.

ii) The two pumps are orthogonal to the two generated photons, these processes are related to the χ_{xxyy} (or χ_{yyxx}) tensor element.

iii) The two pumps are orthogonal between them and the same for the generated photons, these processes are related to the χ_{xyxy} (or χ_{yxyx}) tensor element.

The most efficient process comes from χ_{xxxx} (χ_{yyyy}) because $\chi_{xxxx} = \chi_{xxyy}+\chi_{xyyx}+\chi_{xyxy}$.

In the present work the case ii) will be considered, where the x axis will be related to the slow axis and the y axis will be related to the fast axis, see figure 5.3. It is important

to highlight that the cross-polarized SFWM process implies a shift in wavelength of $\delta = 2\omega_{pump}\Delta/c$ over the co-polarized process, where Δ is the birefringence. This shift has the advantage of displace the $\omega_{s,i}$ with respect of ω_{pump}, such that Raman noise can be avoided.

The photon pairs generated by SFWM process exhibit spectral and temporal correlations, and if the conditions are suitable, correlations in transverse structure can also be present. In order to foster the correlations in transverse structure it is required that the optical fiber supports more than one mode.

3.1 Spontaneous Four-Wave Mixing State

In order to derive an expression for the SFWM state it is necessary to know the interaction Hamiltonian of the system and apply the standard quantum dynamics theory. The electromagnetic field energy in a given volume $\mathbf{V}$ is expressed as

$$H = \frac{1}{2}\int_{\mathbf{V}} dV\ (W_e + W_m), \tag{3.2}$$

where $W_e = E_i D_i$ and $W_m = H_i B_i$ are the electric and magnetic energy density respectively, and $\mathbf{V}$ is the interaction volume. The displacement fields are given in terms of the total electric field and polarization for the electric displacement case and in terms of the magnetic field and magnetization for the magnetic displacement case

$$D_i = \epsilon_0 E_i + P_i, \tag{3.3}$$

$$H_i = \frac{1}{\mu_0} B_i - M_i, \tag{3.4}$$

where ϵ_0 is the vacuum permittivity, μ_0 is the vacuum permeability, P_i is the ith polarization component and M_i is ith the magnetization component. The optical fiber are nonmagnetic medium then the magnetization is null [33].

For third order nonlinear processes such as SFWM, the polarization only includes the first and third order terms $P_i = \epsilon_0[\chi^{(1)}_{ij}E_j + \chi^{(3)}_{ijkl}E_jE_kE_l]$, then the electric energy density can be written as

$$W_e = \epsilon_0 \left((1 + \chi^{(1)}_{ij})E_iE_j + \chi^{(3)}_{ijkl}E_iE_jE_kE_l \right). \tag{3.5}$$

The total electric field has four terms $E_j = E_{1j} + E_{2j} + E_{sj} + E_{ij}$ corresponding to the two pump photons 1 and 2, and the two generated photons s and i. Each electric field can be written in a positive and negative frequency part $E_\mu = \frac{1}{2}(E^{(+)}_\mu + E^{(-)}_\mu)$ where $\mu = 1,\ 2,\ s,\ i$. Considering the previous expression for the electric field and the electric energy density equation (3.5), it can be derived that the term associated with the SFWM process is given by

$$W_{SFWM} = \frac{3}{8}\epsilon_0\chi^{(3)}E^{(-)}_1E^{(-)}_2E^{(+)}_sE^{(+)}_i, \tag{3.6}$$

where $\frac{3}{8}\chi^{(3)}$ represents the $\chi^{(3)}_{xxyy}$ element involved in the process, it has also been considered that two pump photons are annihilated and two photons are generated in the process.

Considering the electric energy density for the SFWM process equation (3.6), the Hamiltonian for SFWM process is written as

$$H_{SFWM} = \int_{\mathbf{V}} dV \ \left(\frac{3}{8}\epsilon_0\chi^{(3)}E^{(-)}_{1i}E^{(-)}_{2j}E^{(+)}_{sk}E^{(+)}_{il} + H.C. \right). \tag{3.7}$$

The pump fields can be modeled as classical fields are given by

$$E_{\mu}^{(+)} = A_{\mu} \sum_{p} W_{\mu p} f_{\mu p} \int d\omega_{\mu}\ \alpha_{\mu}(\omega_{\mu}) \exp\left(-i(\omega_{\mu} t - k_{\mu p} z)\right), \tag{3.8}$$

where $\mu = 1, 2$, A_{μ} is the maximum amplitude of the field, α_{μ} is the spectral envelope, $f_{\mu p}$ is the transverse profile, and $W_{\mu p}$ is the pump power fraction coupled, and $f_{\mu p}$ is the transverse profile.

The electric field operator corresponding to the generated photons fields are expressed as [35]

$$\hat{E}_{\nu}^{(-)} = -i\sqrt{\delta k} \sum_{m} \frac{f_{\nu m}^{*}}{\sqrt{\Theta_{\nu m}}} \sum_{k_{\nu m}} \exp\left(i(\omega(k_{\nu m})t - k_{\nu m} z)\right) l(k_{\nu m}) \hat{a}(k_{\nu m}), \tag{3.9}$$

where $\nu = s, i$, $\delta k = 2\pi / L_Q$ is the modes spacing, $f_{\nu p}$ is the transverse profile, also $\Theta_s = \int\int dxdy\ |f_s(x, y)|^2$ and $l(k) = \sqrt{\hbar\omega / \pi\epsilon_0 n_0^2(\omega)}$ have been defined, finally $\hat{a}$ is the annihilation operator.

Once the explicit expression of the Hamiltonian is known, it is possible to determine the SFWM state evolution. The evolution of an arbitrary state $|\psi(0)\rangle$ can be written as

$$|\psi(t)\rangle = \hat{U}(t, 0)|\psi(0)\rangle, \tag{3.10}$$

where $\hat{U}(t, 0)$ is the evolution operator. When the Hamiltonian is time-dependent the operator evolution takes the form of a series [36], the solution to first order is given by

$$\hat{U}^{1}(t, 0) = 1 - \frac{i}{\hbar} \int_{0}^{t} d\tau\ \hat{H}(\tau), \tag{3.11}$$

where $\hat{H}$ is the Hamiltonian operator of the system.

Considering the expression for the evolution operator equation (3.11), the state evolution can be written as

$$|\psi(t)\rangle = \left[1 - \frac{i}{\hbar}\int_0^t d\tau\ \hat{H}(\tau)\right]|\psi(0)\rangle. \tag{3.12}$$

Finally, by replacing the expression for the pump fields equation (3.8) and generated fields equation (3.9) in the SFWM Hamiltonian equation (3.7) and considering the state evolution equation (3.12), the evolution of the SFWM state is written as

$$\begin{aligned}|\psi(t)\rangle_{SFWM} = |0\rangle_s|0\rangle_i + \sum_{j=1}^{N}\sqrt{W_{j1}W_{j2}}\mathcal{O}_j(\alpha_{j,\beta_j,\mu_j,\nu_j})\times \\ \int\int d\omega_s d\omega_i\ f_j(\omega_s,\omega_i)\hat{a}^\dagger(\omega_s;\mu_j)\hat{a}^\dagger(\omega_i;\nu_j)|vac\rangle,\end{aligned} \tag{3.13}$$

where j represents a particular process, $\hat{a}^\dagger(\omega_s;\mu_j)$ ($\hat{a}^\dagger(\omega_s;\mu_j)$) is the creation operator for the signal (idler) mode with frequency ω_s (ω_i) propagating in transverse spatial mode μ_j (ν_j), W_{j1} (W_{j2}) is the pump power coupled ... 1 (2), $|vac\rangle$ is the vacuum state, and $\mathcal{O}_j(\alpha_{j,\beta_j,\mu_j,\nu_j})$ is the transverse mode overlap integral between the four waves, which is written as

$$\mathcal{O}_j(\alpha_{j,\beta_j,\mu_j,\nu_j}) = M_j\int d^2\rho^\perp\ g(\alpha_i,\rho^\perp)g(\beta_i,\rho^\perp)g^*(\mu_i,\rho^\perp)g^*(\nu_i,\rho^\perp), \tag{3.14}$$

where $g(\xi,\rho^\perp)$ is the transverse electric field distribution for transverse mode ξ and transverse position $\rho^\perp$, and M_j is a normalization constant.

For process j, $f_j(\omega_s,\omega_i)$ represents the joint spectral amplitude (JSA)

$$f_j(\omega_s,\omega_i) = \int d\omega\ A(\omega)A(\omega_s+\omega_i-\omega)sinc\left[\frac{L}{2}\Delta k_j\right]\exp\left(i\frac{L}{2}\Delta k_j\right), \tag{3.15}$$

where L is the fiber length, $A(\omega)$ is the (degenerate) pump spectral envelope and Δk_j

represents the phase mismatch given by 3.1. The JSA is related to the joint spectral intensity (JSI) by

$$I_j(\omega_s, \omega_i) = |f_j(\omega_s, \omega_i)|^2. \tag{3.16}$$

All the information about the photon pair state is basically contained in the joint spectral amplitude. It is important to note that information about the phase present in the joint spectral amplitude is lost in the joint spectral intensity.

3.1.1 State Engineering

From the JSA function 3.15 can be understood how the different parameters control the two photon state. When a particular behaviour of the photon pair is desired it is necessary to choose the fiber and pump properties appropriately to obtain it.

In figure 3.2 the JSI function for different kinds of correlation in the photon pairs is shown. Those JSI correspond to numerical simulations considering a Gaussian pump centered at $690nm$ with bandwidth $\sigma = 1.6813THz$, in a birefringent fiber with core $r_{core} = 1.45\mu m$, numerical aperture $NA = 0.2$, birefringence $\Delta = 2.38 \times 10^{-4}$ and fiber lengths $L = 30cm$, $15cm$, $7cm$. For calculate the JSI, has been considered that all the waves are propagating in the LP_{01} mode. The figure 3.2 shows the great versatility of the SFWM photon sources based in optical fiber, because modifying only the fiber length results in a control over the two photon correlation. A similar two photon correlation control can be obtained varying other parameters.

From equation (3.15) it can be noted that it is not possible in general to write the SFWM JSA as a product of a pump spectral envelope function and a phasematching function as is the case for SPDC [38], but under certain considerations and taking

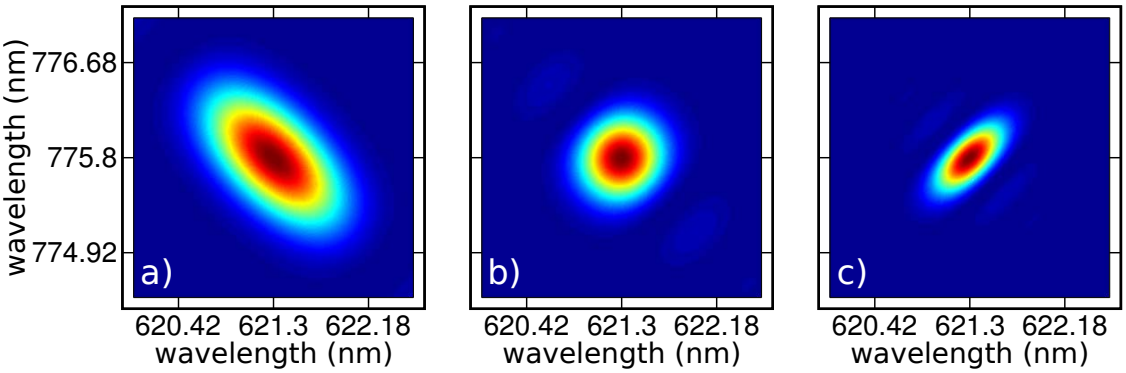

Figure 3.2: Joint Spectral Intensity for a specific fiber and different lengths showing a)Negative correlation, b)Nearly-vanishing correlation and c)Positive correlation. The correlation changes with the fiber length only.

specific spectral regions it becomes possible [15]. The procedure consists in write the two pump spectral envelopes $\alpha(\omega)$ as Gaussian functions with bandwidth σ centered at ω_p and considering a linear approximation for the phase mismatch. To assume that each process j is phasematched at signal (idler) frequencies ω_{sj} (ω_{ij}), and defining detuning variables $\nu \equiv \omega_\lambda - \omega_{\lambda j}$, with $\lambda = s, i$, the JSA correct to first order in ν_s and ν_i can be written as

$$f_j(\nu_s, \nu_i) = \alpha(\nu_s, \nu_i)\phi(\nu_s, \nu_i), \tag{3.17}$$

in terms of the pump spectral envelope α and the ϕ_j phasematching function for the jth process. Such functions are written as

$$\alpha(\nu_s, \nu_i) = \exp\left(-\frac{(\nu_s + \nu_i)^2}{2\sigma^2}\right), \tag{3.18}$$

$$\phi_j(\nu_s, \nu_i) = \exp\left(-x^2/D\right)[erf(D/2 - ix/D) + erf(ix/D)], \tag{3.19}$$

where, $L\Delta k \approx T_s\nu_s + T_i\nu_i \equiv x$ is an adimensional phase mismatch and $erf(\cdot)$ is the error function. The parameters D and T_μ follow the definitions

$$D = \sigma L(k_1' - k_2')/\sqrt{2}, \tag{3.20}$$

$$T_\mu = L\left[\frac{k_1' + k_2'}{2} - k_\mu'\right] \quad \text{with} \quad \mu = s, i, \tag{3.21}$$

where a prime denotes a frequency derivative evaluated at ω_p for the pumps and at ω_{sj} (ω_{ij}) for the signal (idler); k_λ (with $\lambda = 1, 2, s, i$) is the wavenumber for each wave. D represents a non-degeneracy parameter, with $|\phi(x)| = sinc(x/2)$ at degeneracy ($D \to 0$).

Now it is possible to discriminate the pump spectral envelope function and the phasematching function contribution to the JSA function. In figure 3.3 plots of the two functions along with their product are shown. Those numerical simulations consider the same parameters mentioned previously for figure 3.2 and a fiber length of $L = 15cm$.

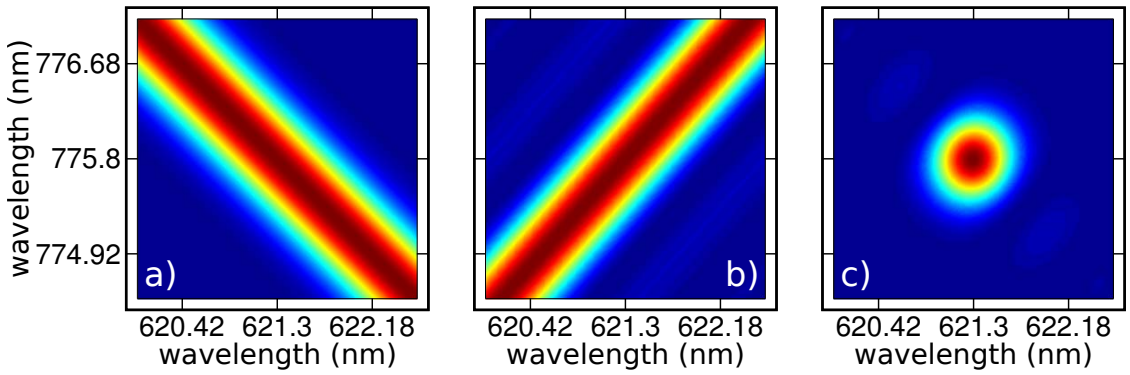

Figure 3.3: Numerical Joint Spectral Intensity decomposed. a) Pump spectral envelope $|\alpha(\nu_s, \nu_i)|^2$, b) Phasematching $|\phi(\nu_s, \nu_i)|^2$, c) JSI $|\alpha(\nu_s, \nu_i)\ \phi(\nu_s, \nu_i)|^2$

In this way the desired spectral correlation of the photon pair can be searched con-

sidering the weight of the pump and phasematching factors separately.

3.1.2 Schmidt Decomposition

The Schmidt decomposition is a tool which can be used to quantify the degree of entanglement of a two photon system. It consists of expressing a bipartite system in terms of a complete set of orthonormal basis states [39, 40], which are eigenstates of the bipartite system. Such a decomposition is unique.

From equation (3.13) the two photon state is written as

$$|\psi\rangle = \int\int d\omega_1 d\omega_2 \; f(\omega_1, \omega_2)\hat{a}^\dagger(\omega_1; \mu_j)\hat{a}^\dagger(\omega_2; \nu_j)|vac\rangle. \tag{3.22}$$

The fields associated with the two photons are entangled if $f(\omega_s, \omega_i)$ cannot be factorized into a product of functions of ω_1 and ω_2 as $f(\omega_s, \omega_i) = g(\omega_s) * h(\omega_i)$. Performing the Schmidt decomposition for $f(\omega_s, \omega_i)$ leads to

$$f(\omega_1, \omega_2) = \sum_i \sqrt{\lambda_i}\phi_i(\omega_1)\varphi_i(\omega_2), \tag{3.23}$$

where the Schmidt coefficients $\sqrt{\lambda_i}$ satisfy the normalization condition $\sum_i \lambda_i = 1$ and the orthonormal basis states ϕ and φ are the Schmidt modes. The function $f(\omega_s, \omega_i)$ is factorable if there is only one term on the right side of equation (3.23). Therefore, the bipartite system is entangled if the number of nonzero eigenvalues is more than one.

Using the Schmidt decomposition of $f(\omega_s, \omega_i)$ the two photon state can be rewritten as

$$|\psi\rangle = \sum_i \sqrt{\lambda_i}\hat{b}^\dagger(\omega_1; \mu_j)\hat{c}^\dagger(\omega_2; \nu_j)|vac\rangle. \tag{3.24}$$

The number of elements required in the sum to express $f(\omega_s, \omega_i)$ in terms of the Schmidt modes is related to the degree of factorability of the two-photon state. The Schmidt coefficients defines the Schmidt number as

$$K = \frac{1}{\sum_i \lambda_i^2}, \tag{3.25}$$

the number K indicates how many frequency Schmidt modes participate in the two-photon state and therefore is an entanglement measure. The Schmidt number is related to the purity according to

$$P = \frac{1}{K}. \tag{3.26}$$

Photon pairs with purity $P = 1$ are such that only a single Schmidt mode is active.

Chapter 4

Performing of the Mode Selective Photonic Lantern

The photonic lantern is a technology that has emerged from the astrophotonics field. Nowadays the main applications are focused in multiplexing signals, but due to the capacity to modify the transverse structure of light, they are also used as beam shapers.

A mode selective photonic lantern (MSPL) is a passive component that allows the conversion of multi-mode signals into multiple single-mode signals and vice versa. The basic scheme for a MSPL consist of several single-mode ports in one end and a single multi-mode port in the other end. The group of single-mode ports can be seen as a m degenerate multi-mode system, meanwhile the multi-mode port as a non degenerate system with m modes. In the MSPL the light transits from the degenerate system to the non degenerate one via a transition, if the transition is adiabatic the supermodes of the first array evolve into the modes of the second, and vice versa [31, 32]. In figure 4.1 a mode selective photonic lantern scheme is shown

A MSPL applies a transformation that maps input orthogonal sets to output orthog-

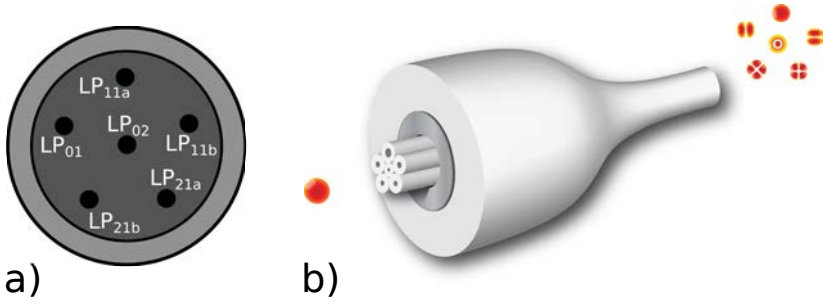

Figure 4.1: 6 terminal mode selective photonic lantern. a)Inputs. b)Scheme.

onal sets. If the number of inputs and modes is the same and the system is (approximately) lossless the transformation can be linear [41]. The relation between the input and output in the lantern can be written as

$$A_{ij}v_j = u_i, \tag{4.1}$$

where A_{ij} is the transfer matrix of the lantern, v_j is a basis vector in the degenerate multimode system and u_i is a base vector in the non degenerated system.

There are several schemes used to manufacture this kind of devices: SMF + Holey cladding, SMF + Solid cladding, Multicore fiber + Solid cladding, Written Integrated Waveguide Chip, among others. In figure 4.2 are shown some photonic lantern schemes. In the present work a scheme SMF + Holey cladding will be employed [42].

One explanation of the photonic lantern operation is based in an analogy of a single-electron in 1D potential (Kronig-Penney model) [31].

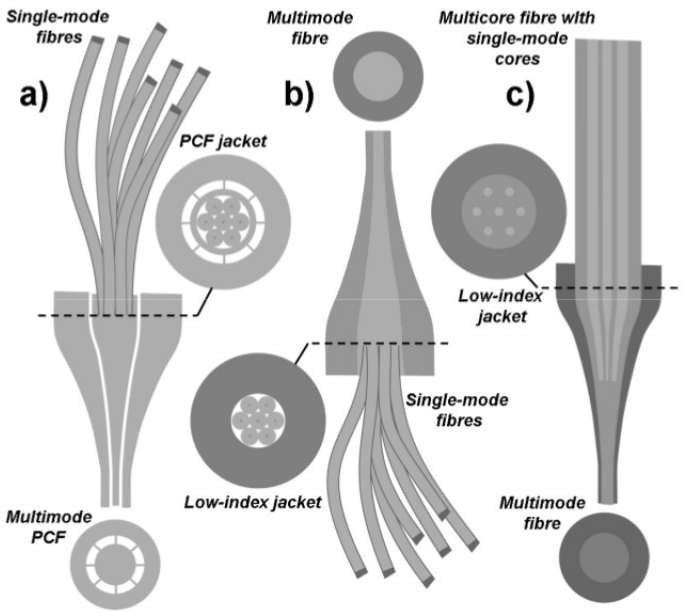

Figure 4.2: Several photonic lantern schemes

Chapter 5

Spontaneous Four Wave Mixing in Birefringent Optical Fiber

In the next lines it will be described the generation of photon pairs using birefringent optical fibers, first the source preparation will be discussed, and then the characterization of the photon properties.

5.1 Source Preparation

In figure 5.1 the experimental setup to prepare the source is shown. A tunable picosecond mode-locked Ti:sapphire laser (Coherent MIRA 900-D) was used as pump, with $76MHz$ repetition rate, $0.52nm$ bandwidth approximately, and TEM_{00} spatial mode. The pump spectrum was cleaned with the help of a prism based filter (PBF) composed of: two $7.5cm$ lenses (Thorlabs LA1257-B), two Brewster prisms (Thorlabs AFS-SF14) and one slit made from two razor blades. The spectral window of the filter was set to transmit about $10nm$ and has a power transmittance of 80%. The pump polariza-

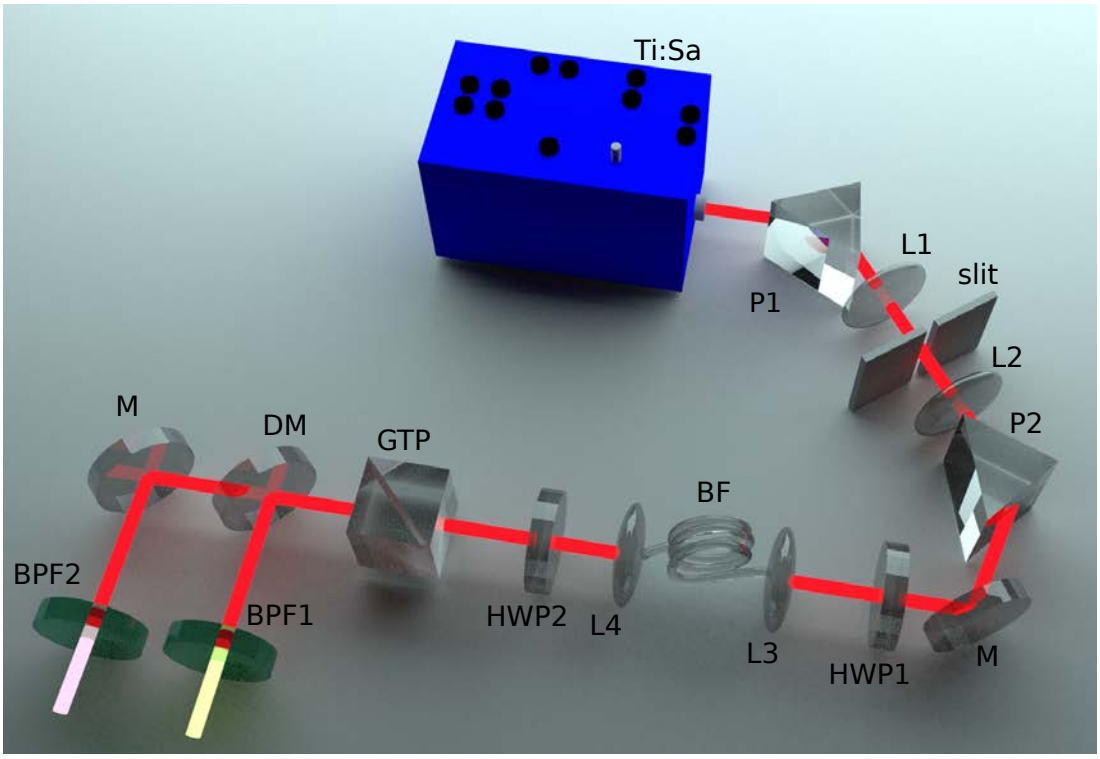

Figure 5.1: Source preparation.

tion was adjusted parallel to the slow axis of the fiber with a half wave plate (HWP1) (Thorlabs AHWP05M-600).

The coupling of pump light into the core of the fiber was prepared in such a way that other modes besides the fundamental mode were excited and guided inside the fiber. In figure 5.2 the spectral behavior of the pump is shown. An average power of $50mW$ was coupled using an $8mm$ aspheric lens (Thorlabs C240TME-B), then another $8mm$ aspheric lens was used to out-couple the light.

A cross polarized phase matching scheme was implemented, where the pump and generated photons are mutually orthogonal between them figure 5.3. The pump photons were suppressed using one half wave plate (HWP2) (Thorlabs AHWP05M-600) followed by a Glan-Thompson polarizer (GTP) (Thorlabs GTH5), this combination gave a pump

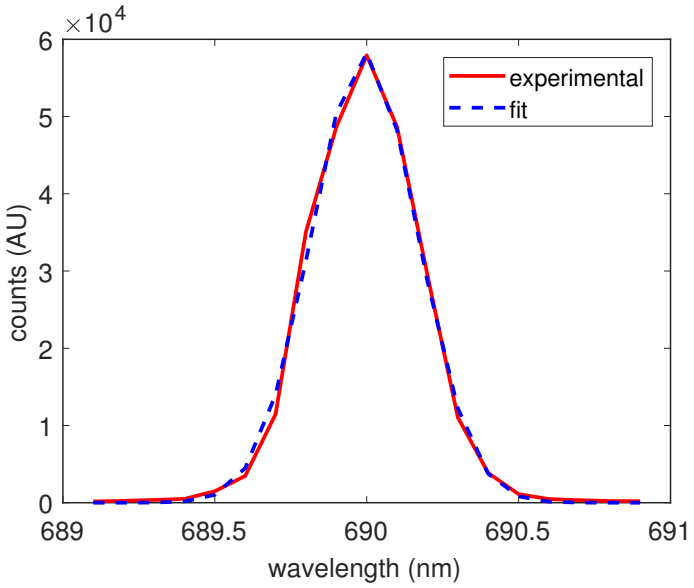

Figure 5.2: Experimental pump spectrum centered at $690nm$ (red) and numerical fit (blue).

suppression factor of around 96%.

Since the signal and idler generated photons are spectrally non degenerated a dichroic mirror (DM) (Semrock FF685-Di02-25x36) was used to split them, the photons with wavelength higher than $676nm$ are transmitted with 93% probability meanwhile the ones with wavelength lower than $695nm$ are reflected with 98% probability. Adequate bandpass filters were placed to suppress the remaining pump, for the arm with lower wavelength a band pass filter (Semrock FF01-630/92-25) with 92% of transmittance in the range $584 - 676nm$ was used, in the case of the arm higher wavelength a band pass filter (Semrock FF02-809/81-25) with 93% of transmittance in the range $768.5 - 849.5nm$ was used.

As nonlinear medium two different birefringent fibers were employed: bow-tie *HB800G* and *HB800C*. In figure 5.1 the transverse profiles of the fibers used are shown. Both fibers have the same general structure but the main difference between them consists in

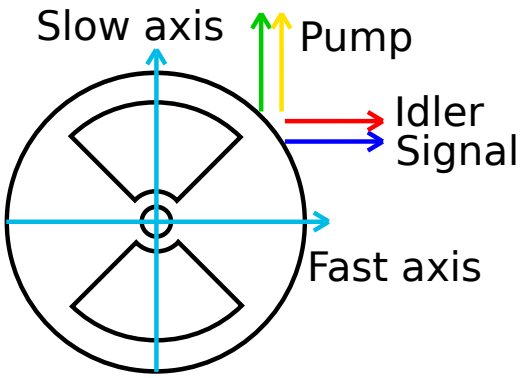

Figure 5.3: Scheme of cross polarized SFWM in the bowtie fiber profile. The pump polarization is parallel to the slow axis of the fiber and the polarization of the generated photons is parallel to the fast axis.

the separation of the core and the stress applying elements in each fiber. This difference was fundamental for the modeling of the SFWM sources, as is discussed below.

5.2 SFWM in *HB800G* Fiber

The first fiber used was the bow-tie *HB800G*, with a length of $12cm$. The characteristics of the pump and the fiber were selected to allow higher order modes can propagate inside the fiber.

5.2.1 Spectral Response

Once the photon pairs have been generated it is necessary to characterize their properties. The first step of the characterization consists of resolving the spectral behavior, the setup is shown in figure 5.5. The two arms were coupled into two multi-mode fibers respectively (MMF1 and MMF2) (Thorlabs M43L02) using $8mm$ aspheric lenses, with a coupling efficiency of about 95%. In order to detect the generated photons, the signal

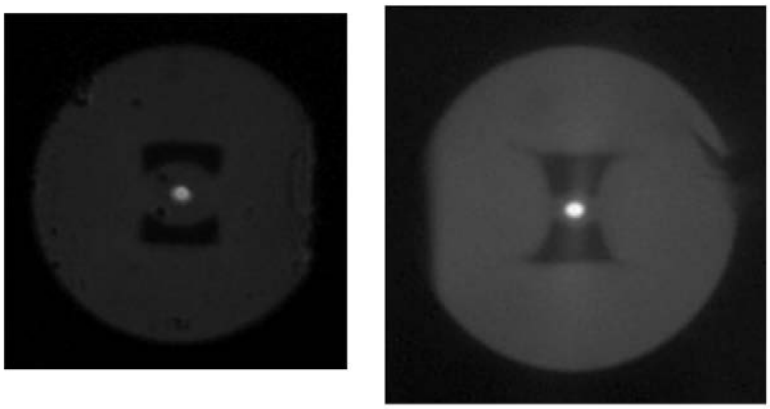

Figure 5.4: Fiber transverse profile of a)*HB800G* and b)*HB800C*.

(idler) arm could be directed to a Czerny-Turner monochromator (CTM) (Andor Shamrock 500i) with its output port fitted to a silicon avalanche photodiode (APD2) (Perkin Elmer SPCM-AQR-14-FC) with a multimodal fiber (Thorlabs M43L02). Alternatively, the signal (idler) arm could be directed to a silicon avalanche photodiode (APD1). In this way the photons could be detected with spectral resolution or directly. The light transmission of the complete monochromator-optical fiber system was about 5%. In order to perform the coincidence measurements the signal (idler) arm fiber is directed to the monochromator, while the idler (signal) arm is directed to photodiode.

In each photodiode a TTL (transistor-transistor logic) pulse of $2.5V$ height and a $17ns$ width is generated when a photon is recorded. Each photodiode signal is split in two parts, one half is used to record single counts and the other half is used to obtain coincidence counts. The electrical signals were recorded with a connector block (National Instruments BNC-2121) fitted to a counter/timer device (National Instruments PCIe-6612). The coincidences were obtained sending a half signal from each photodiode to a nuclear instrumentation module (NIM) (ortec 4001C). Previous to reaching the NIM the

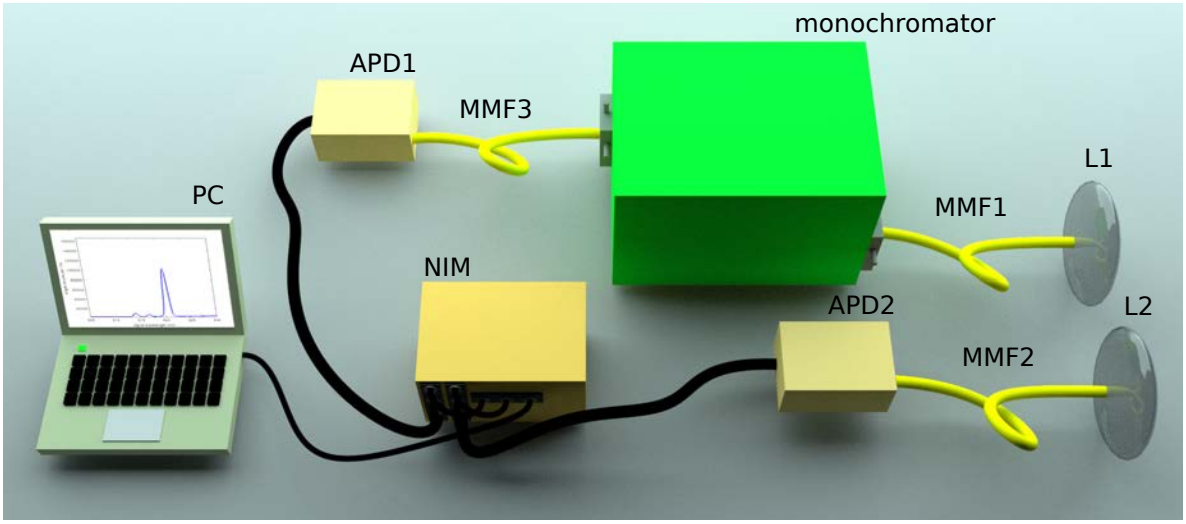

Figure 5.5: Detection scheme to resolve spectral behaviour.

two signals were attenuated with an attenuator (Pomona 4108-20DB) and inverted with an inverting pulse transformer (Phillips Scientific 460) to become them compatible with NIM. Every half APD signal was discriminated using a discrimination module (Phillips Scientific 704), a threshold voltage equal to 80% of $1.25V$ was set to reduce noise signals with voltages lower than it, also the output pulse width was set to $5ns$. The signal that came from APD1 was sent toward a delay module (Phillips Scientific 792), making it possible to control the relative delay between the two signals. Both signals were then sent to a coincidence module (Phillips Scientific 704), a coincidence was recorded when both signals overlapped within a time window of $10ns$, that window is given by the sum of the two pulse widths. Adjusting the relative delay between the two signals the total (raw) coincidence counts were obtained. In order to discriminate noise in coincidence counts, also were taken the coincidences with an additional delay in the arm coming from APD1 equal to the pump period ($13ns$), these counts are referred as accidental coincidence counts. Finally, the accidental coincidence counts are subtracted from total

coincidences counts. In order to control the monochromator central wavelength and perform the single and coincidence counts recording, a LabView program was developed.

In figure 5.6 are shown the spectra obtained for *HB800G* fiber. The first row displays the single counts recorded in $10s$ for both arms, it is possible identify four pairs of peaks that conserve energy. The peaks were labeled as I, II, III and IV. A broad background appears in both arms, possibly due to Raman processes. In the second row the total and accidental coincidence counts in $10s$ are presented. The Raman signal decrease when recording coincidence counts. In the third row the accidental-subtracted coincidence counts in $10s$ are presented. Note that the Raman signal is essentially suppressed. The presence of multiple peaks suggests that multiple SFWM processes occur in the fiber.

5.2.2 *HB800G* Fiber Discussion

The spectral measurements for *HB800G* optical fiber shown in figure 5.6, suggest four different SFWM processes occurring simultaneously at the pump wavelength $690nm$. For each SFWM process in figure 5.6, there is a specific combination for transverse mode and wavelength for each of the four waves involved. Furthermore, the processes are not spectrally degenerate, making feasible to address each process separately by means of spectral filtering.

In order to describe the processes observed in figure 5.6 a numerical simulation was implemented, the first step is to know the possible processes that fulfill the phasematching condition in the *HB800G* optical fiber. The dispersion for the *HB800G* fiber was modeled according to the equation (2.13), where a step index fiber contribution and a birefringence contribution are considered. Under that approach three parameters (r_{core}, NA, and Δ) are necessary to determine the wavenumber $k_{lm,\mu} = n_{lm,\mu}(\omega)\omega/c$ for a LP_{lm} mode and for a μ polarization given. It is necessary to keep in mind that the

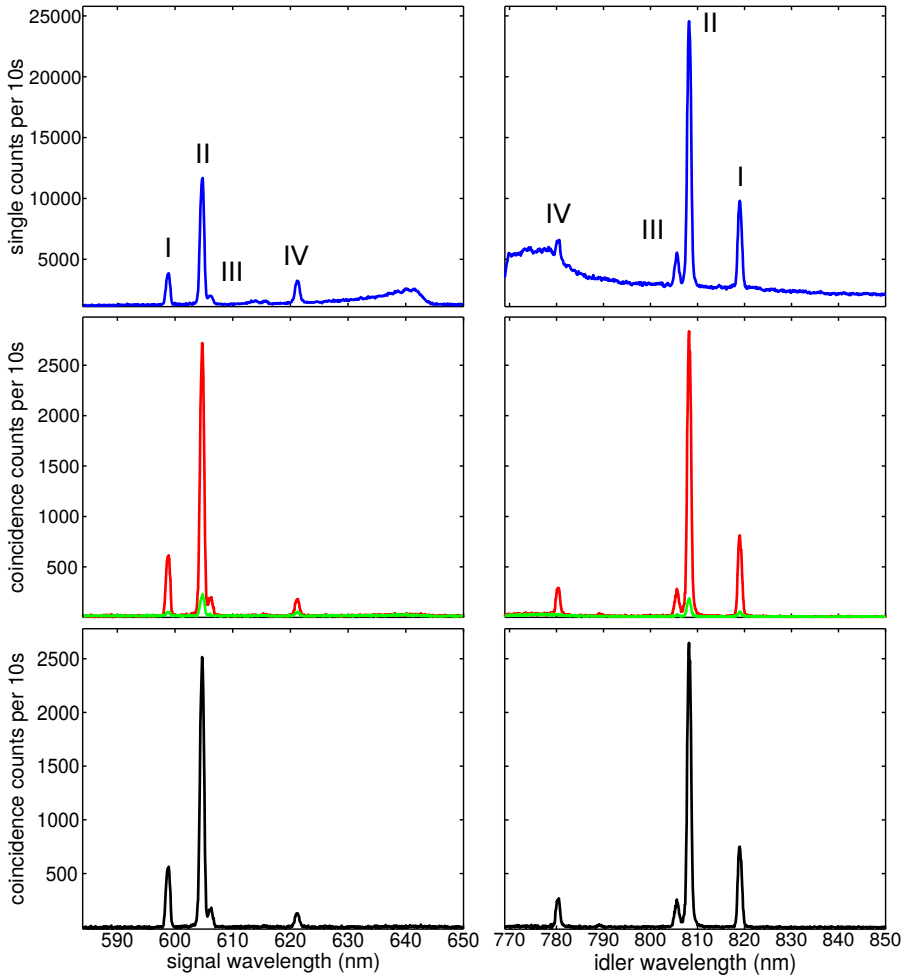

Figure 5.6: First row shows single counts (blue). Second row shows total (red) and accidental (green) coincidence counts. Third row shows accidental-subtracted coincidence counts (black).

process	p_1	p_2	i ($\lambda < \lambda_p$)	s ($\lambda > \lambda_p$)
A	LP_{01}	LP_{01}	LP_{01}	LP_{01}
B	LP_{11}	LP_{11}	LP_{11}	LP_{11}
C	LP_{01}	LP_{11}	LP_{11}	LP_{01}
D	LP_{01}	LP_{11}	LP_{01}	LP_{11}
E	LP_{21}	LP_{21}	LP_{21}	LP_{21}
F	LP_{01}	LP_{21}	LP_{21}	LP_{01}
G	LP_{11}	LP_{21}	LP_{21}	LP_{11}

Table 5.1: Mode combination that allow SFWM processes in the *HB800G* optical fiber.

real refraction index is azimuthally dependent and the model used was a simplification. Considering the values of the parameters r_{core} and NA of the *HB800G* optical fiber given by the manufacturer, it can be determined that the LP_{01}, LP_{11} and LP_{21} are supported in the fiber for the frequencies considered.

Now, it is possible explore the { r_{core}, NA, Δ } space to determine the values of the parameters that best fit the experimental SFWM data. The parameters were varied within the ranges $1.4\mu m < r_{core} < 2.5\mu m$, $0.14 < NA < 0.3$ and $4.0 \times 10^{-4} < \Delta < 5.0 \times 10^{-4}$ respectively to generate numerical phasematching curves. The strategy consisted in to identify the maxima of the experimental peaks, then to choose values of the fiber parameters (Δ, r_{core}, and NA) to generate the numerical curves. The parameter Δ was left fixed and the space { r_{core}, NA } was explored every time. The numerical curves were generated looking for the condition $\Delta k_{pqmn} = 0$ on one hand, and on the other hand the matching with the experimental maxima. The values of the parameters that generate numerical curves such that a quadruple intersection with the experimental peaks is obtained, are considered as candidates to explain the fiber. In the table 5.1 are listed the seven possible processes that best explain the SFWM peaks measured for the *HB800G* optical fiber, for each process the condition $\Delta k_{pqmn} \approx 0$ is present, in addition the overlap of the four transverse modes has an appreciable value.

From the numerical simulation was obtained that only the combination of processes A, B, G and C or A, B, G and F can explain the experimental peaks I, II, III and IV, respectively. Moreover, it were found the values of the parameters: $r_{core} = 1.6 \pm 0.1 \mu m$, $NA = 0.27 \pm 0.2$ and $\Delta = (4.2 \pm 0.1) \times 10^{-4}$ are the best ones. The values of r_{core} and Δ are in concordance with those provided by manufacturer, however the NA value is outside of the range provided.

The figure 5.7 shows the comparison between numerical simulation and experiment. In the first row are shown the phasematching curves $\Delta k_{pqmn} = 0$ for each process listed in table 5.1, the vertical axis corresponds to the pump wavelength and the horizontal axis is related with the wavelength of the generated photon pairs. A dotted line indicates the pump wavelength $692nm$. The second row shows the experimental (purple) and numerical (black) spectra. The curves have been labeled with the associated process and every peak has been labeled with the associated transverse mode. From figure 5.6 it is possible to note that the experimental peaks have different heights, that characteristic can be explained in terms of the process efficiency. The process efficiency has a contribution due to the overlap of the four transverse modes, furthermore, the pump power coupled to every mode is another fundamental parameter. Although it is not possible modify the overlap of the four transverse modes, by controlling the relative pump power coupled to the different modes, it is possible foster the SFWM processes.

In order to understand the discrepancy between the values of the numerical aperture obtained and the one provided by manufacturer, the refractive index profile of the fiber was analyzed. In figure 5.8 is shown the relative refractive index (referred to SiO_2) profile along the fiber as measured by Fibercore Ltd., at a wavelength of $670nm$ for the specific batch of *HB800G* fiber used. Considering the numerical aperture is described as in equation (2.1) and assuming the cladding refractive index as the refractive index

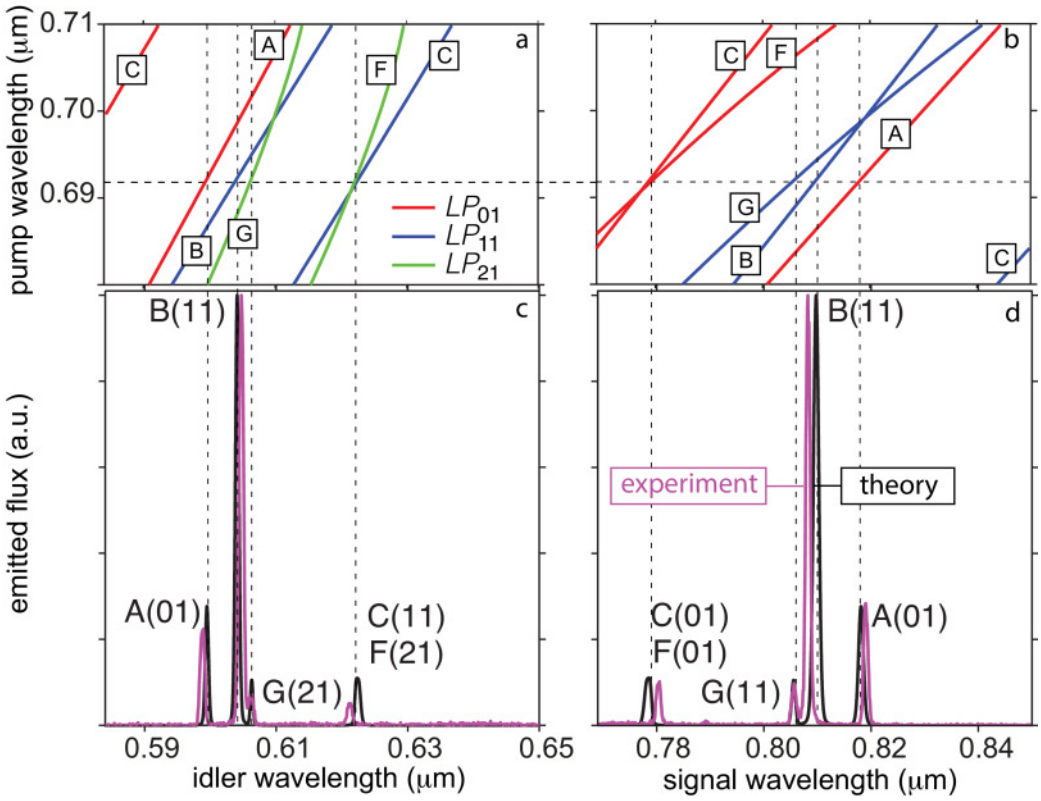

Figure 5.7: Comparison between experimental results (purple) and numerical simulations (black) for *HB800G* optical fiber.

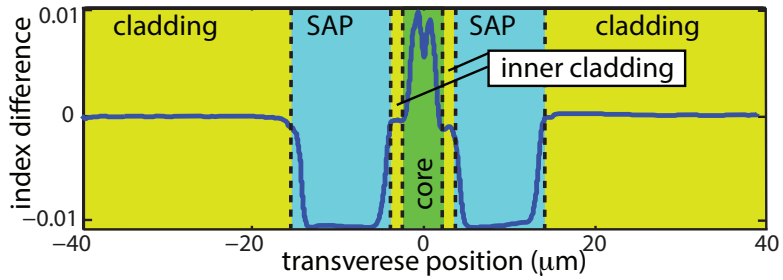

Figure 5.8: Refractive index profile for *HB800G* optical fiber.

of the stress applying parts (SAPs), a value $NA \approx 0.24$ is obtained, this value is closer to the value obtained. That result suggests that the guided mode is in fact large enough to reach the inner portions of the SAPs, introducing an ambiguity in the numerical aperture value and complicating the description of the SFWM processes in the fiber. It is important to note that Fibercore Ltd. has no evidence that the guided mode can reach the inner portions of the SAPs.

Despite the good agreement between experimental and numerical curves, it is challenging to describe this type of fiber due to the short separation between the core and the SAPs, and also possible mistakes considering the numerical aperture can occur. The strategy to avoid problems when considering the cladding refractive index, a similar kind of fiber where the SAPs and the core are enough separated was chosen, such that it is not necessary to consider the SAPs refractive index. In the other optical fiber the evanescent tails of the transverse modes are fully contained by the inner cladding.

5.3 SFWM in *HB800C* Fiber

The second fiber used was the bow-tie *HB800C*, with a length of 14.5cm. This fiber was selected to avoid the considerations with respect to the separation of the core and

stress applying rods. The characteristics of the pump and the fiber were selected to allow higher order modes propagate inside the fiber.

5.3.1 Spectral Response

After the photon pairs generation it is necessary to characterize their properties. Again, the first step of the characterization consists of resolving the spectral behavior, the setup is shown in figure 5.5. The scheme to record the single and coincidence counts is identical to the one in the previous section.

The spectral behaviour for *HB800C* fiber is shown in figure 5.9. The results in the first row shows single counts (blue) recorded in $10s$. In the second row are shown coincidence counts, total (red) and accidental (green), in $10s$. Finally, the accidental-subtracted coincidence counts (black) in $10s$, appear in the third row. Three pairs of energy conserved peaks appear, they were labeled as A, B and C, these spectral results suggest multiple SFWM process are occurring simultaneously.

For *HB800C* fiber the spectra were taken for a set of wavelength pumps between $690nm$ to $720nm$, the accidental-subtracted coincidence counts are shown in figure 5.10. The three pairs of peaks are present for all the pump wavelengths, and are shifted to higher wavelengths when pump wavelength increases.

5.3.2 Transverse Mode

The second step of the characterization consisted in measuring the transverse mode of the generated photons, in figure 5.11 the setup is displayed. For this measurement the signal (idler) arm was coupled into a multi-mode fiber (MMF1) and connected to the monochromator that was fitted to an photodiode (APD1), this allowed to select a specific

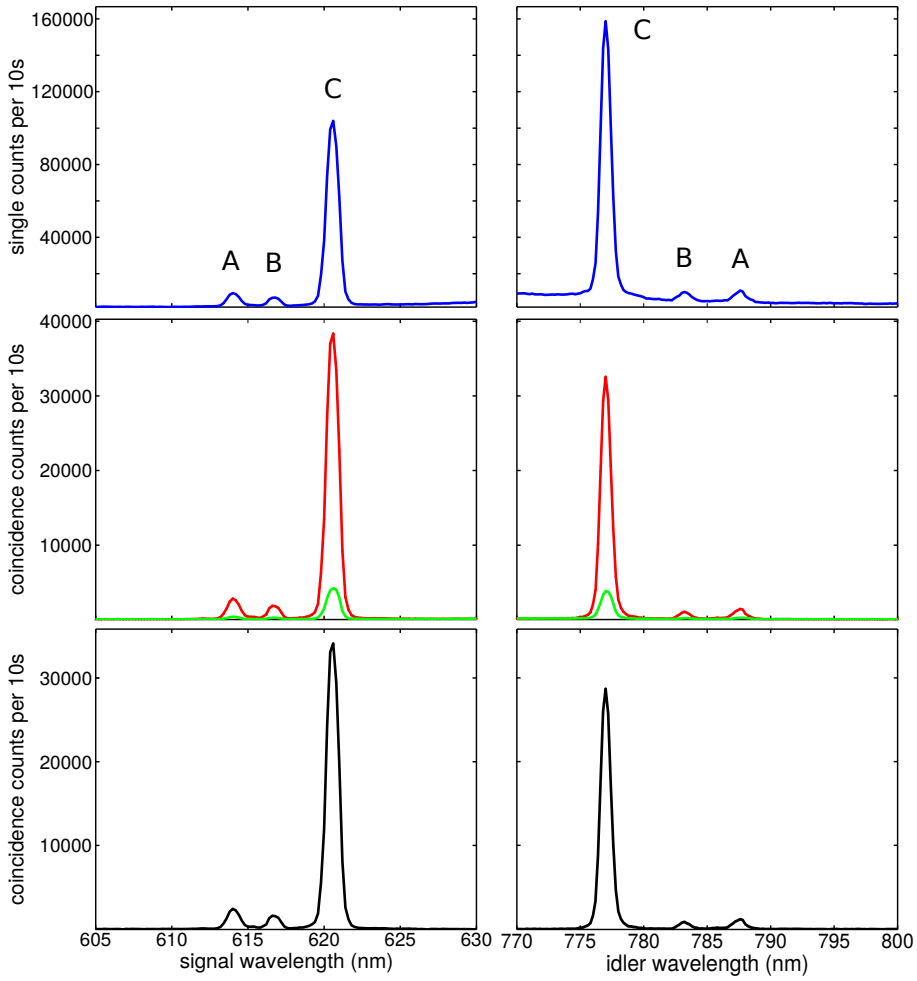

Figure 5.9: First row shows single counts (blue). Second row shows total (red) and accidental (green) coincidence counts. Third row shows accidental-subtracted coincidence counts (black).

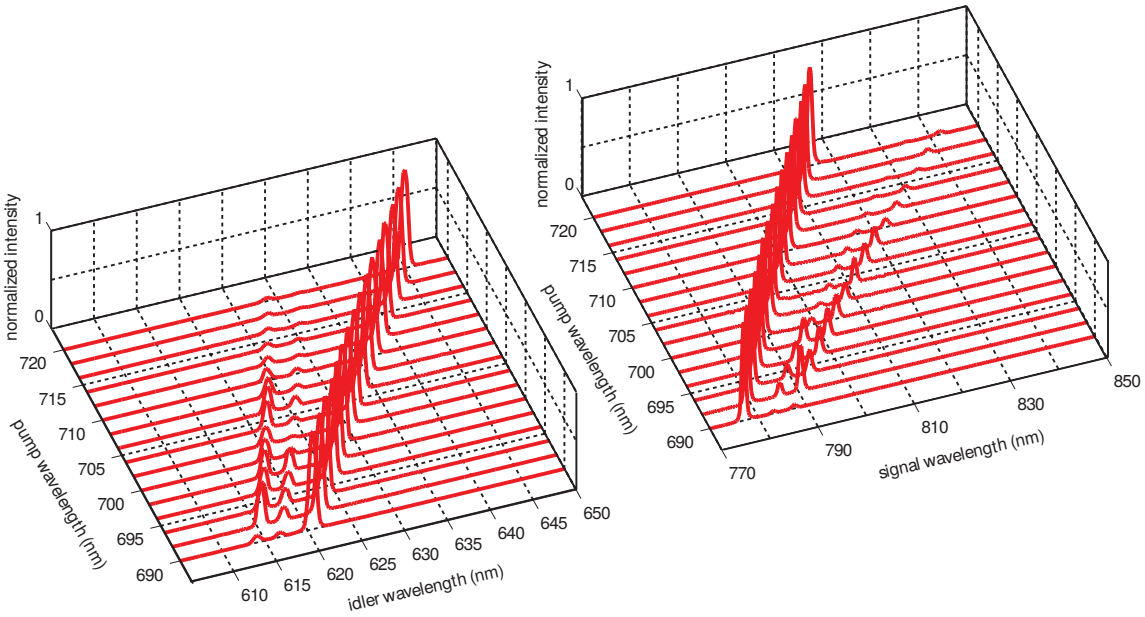

Figure 5.10: Spectral behaviour of the generated photons as a function of pump wavelength for the *HB800C* fiber.

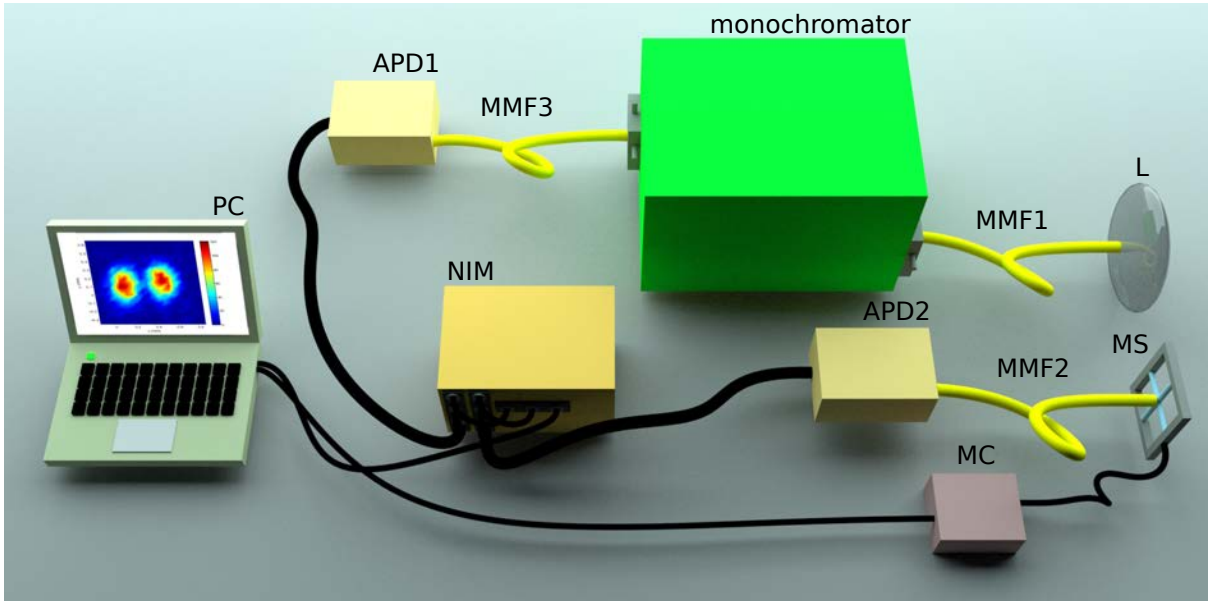

Figure 5.11: Detection scheme to resolve transverse mode.

SFWM process. The signal (idler) arm was used to herald its sibling. The idler (signal) arm was imaged into a plane using the out-coupling $8mm$ aspheric lens, on the plane where the image was formed a fiber tip was mounted, the fiber tip was displaced by a x-y motorized system (Physik Instrumente M-112.1DG) and managed with a controller (Physik Instrumente C-863 mercury servo controller) to rasterize the detection plane. The light collected by the fiber tip was sent to a second photodiode (APD2). The two photodiode signals were processed same way as for spectral measurements described above. For these transverse mode measurements a LabView program was used to control the monochromator central wavelength, the motorized stage displacement and record coincidence counts.

The measurement of transverse modes was carried out for every peak obtained for the *HB800C* fiber, in figure 5.12 are shown the results obtained. From figure 5.12 it can

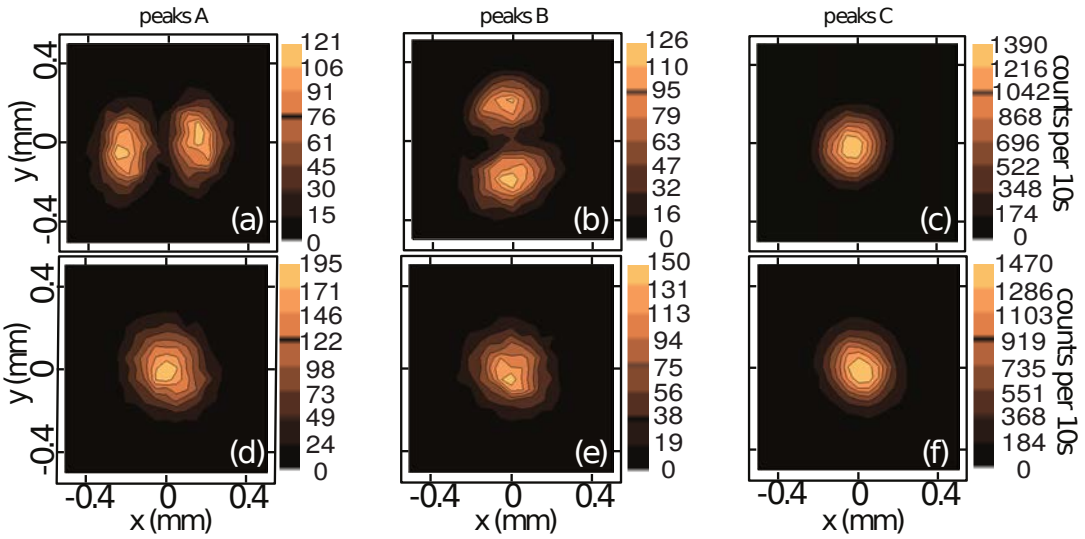

Figure 5.12: The first column shows the transverse modes for generated photons in the process A. The second column shows them for B process. The third column shows them for C process.

be seen that the photons in the lower wavelength arm have access to LP_{11} modes, while the photons in the higher wavelength arm are all in the fundamental LP_{01} mode.

5.3.3 Joint Spectral Intensity

The third and last step of the characterization was to determine the spectral correlation between the photon pair by measuring Joint Spectral Intensity (JSI), in figure 5.13 the setup is shown. Both arms were coupled into identical systems: multi-mode fiber (MMF1/2) directed to a monochromator (monochromator1/2) fitted to a photodiode (APD1/2). In order to take a measurement one monochromator was left fixed at one specific wavelength while the other scanned along a certain spectral range, then the wavelength of the first monochromator changed and the second one scanned again, and so on. The two photodiode signals were processed in the same way as for the previous

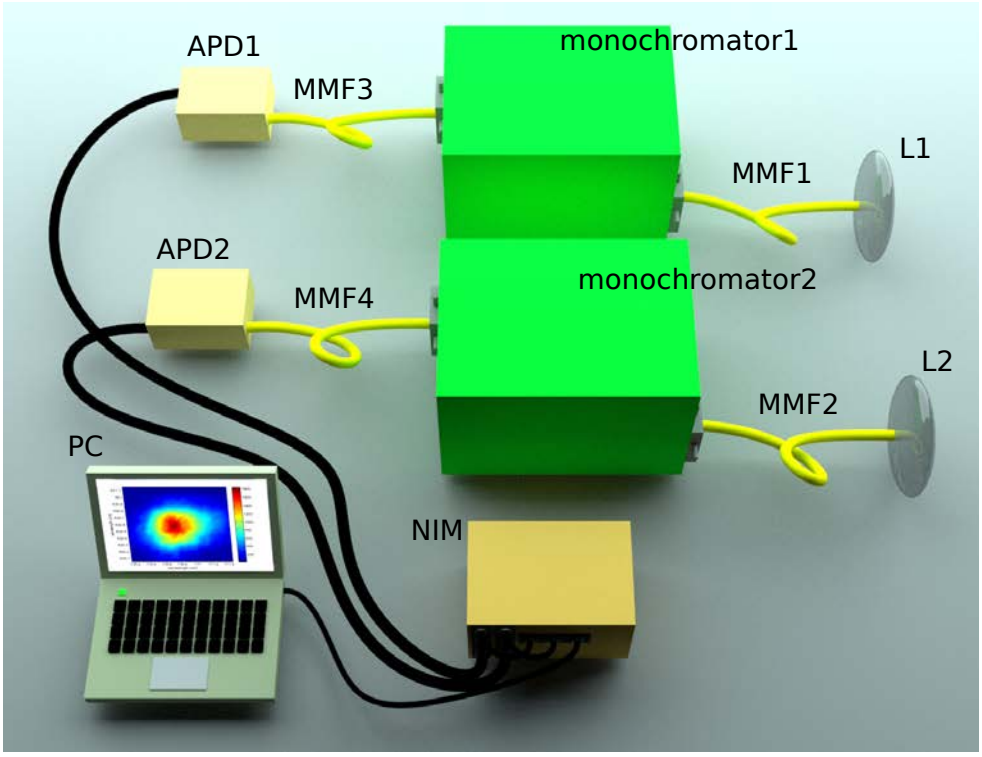

Figure 5.13: Detection scheme to resolve Joint Spectral Intensity.

spectral and mode measurements. A different LabView program was used to control both monochromator central wavelengths and record coincidence counts.

The measurements were performed by choosing neighborhoods around the signal and idler central wavelength of every peak for *HB800C* spectrum. In figure 5.14 are shown the obtained JSI measurements. The JSI measurements of every processes were taken separately, but a single figure with all the three JSIs is also included. All the three processes exhibit nearly non spectral correlation.

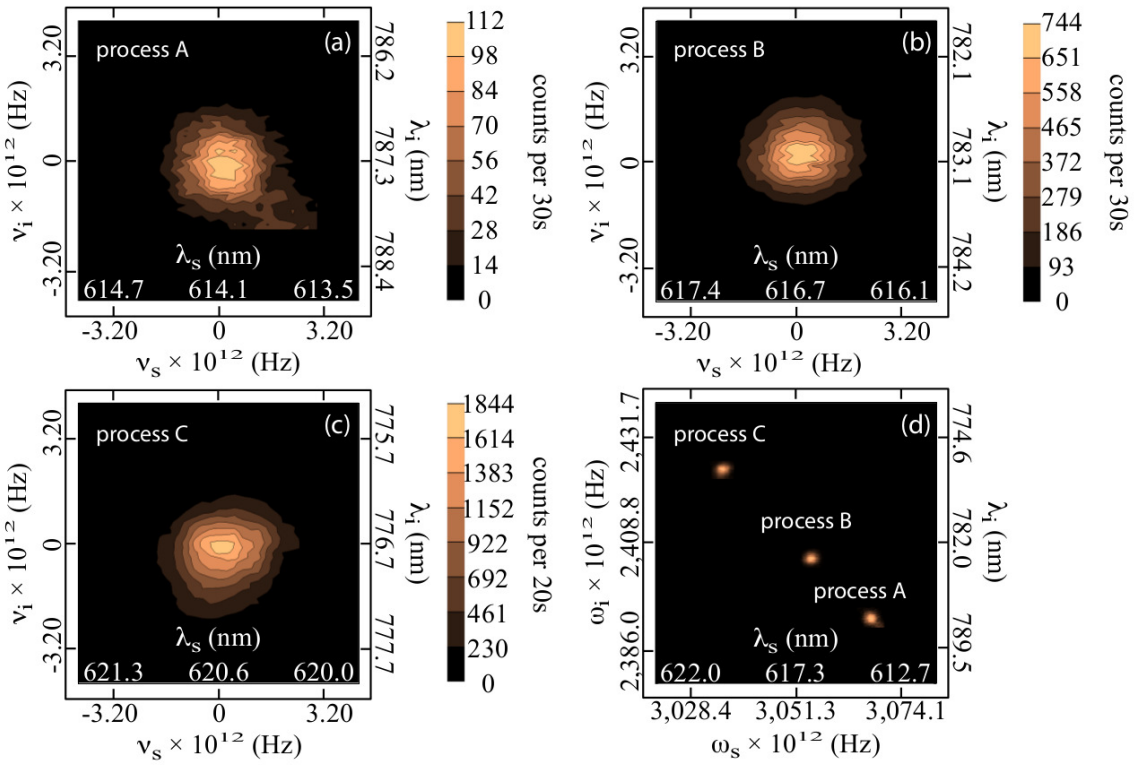

Figure 5.14: Experimental JSI for the three processes (a-c). The three JSI together (d).

5.3.4 *HB800C* Fiber Discussion

The spectral measurements for *HB800C* optical fiber displayed in figure 5.9, suggest that three different SFWM process occur simultaneously for all the pump wavelengths from $690nm$ to $720nm$. The spectral behavior of all the six peaks suffer a shift toward longer wavelengths as the pump wavelength is also increased. For each SFWM process in figure 5.9, there is a specific combination for transverse mode and wavelength for each of the four waves involved. In figure 5.12 it is possible to see the LP_{lm} modes associated with the generated photons, while the modes associated with the pump photons remain unknown. Furthermore, the processes are not spectrally degenerate, making feasible to address each process separately by means of spectral filtering.

In order to describe the processes observed in figure 5.9 a numerical simulation was implemented, the first step is to know the possible processes that fulfill the phasematching condition in the *HB800C* optical fiber. The dispersion for the *HB800C* fiber was modeled according to the equation (2.14), where a step index fiber contribution, a birefringence contribution, and a parity contribution are considered. Under that approach four parameters (r_{core}, NA, Δ, and Δ_p) are necessary to determine the wavenumber $k_{lm,pq} = n_{lm,\mu}(\omega)\omega/c$ for a LP_{lm} mode, for a p polarization and for a q parity given. Again, it is necessary to keep in mind that the real refraction index is azimuthally dependent and the model used was a simplification. The offset Δ_p is implemented because the SAPs break the symmetry of LP modes in the fiber, which implies that modes with different parity are no longer degenerate. Without this additional parameter it is not possible to explain the observed processes within the description adopted. The implementation of this parameter had not been implemented in the literature until the work presented in [37].

By considering the *HB800C* optical fiber manufacturer values of the parameters r_{core}

and NA, and the experimental transverse measurements presented in figure 5.12, it can be determined that the LP_{01} and LP_{11} modes are supported in the fiber. These two modes split into six possible modes, LP_{01}^{x} and LP_{01}^{y} in the case of LP_{01}, and LP_{11}^{ex}, LP_{11}^{ey}, LP_{11}^{ox} and LP_{11}^{oy} in the case of LP_{11}. Where the labels e and o mean even and odd parity respectively, and x and y represent the polarization. Regarding the six possible modes, 6^4 SFWM processes are possible in principle. But, considering only the cross polarized $xx-yy$ processes, conservation of orbital angular momentum and parity, only 15 processes are viable in the fiber [37]. The space $\{\ r,\ NA,\ \Delta,\ \Delta_p\ \}$ was explored to determine the values of the parameters that best fit the measured SFWM data. The parameters were varied within certain ranges to generate numerical phasematching curves. The strategy consisted in to identify the maxima of the experimental peaks, then to choose values of each parameter to generate the numerical curves. The numerical curves were generated employing a genetic algorithm. The genetic algorithm mechanism consists in testing an initial set of solutions, the best solutions are crossed to give rise to a new set of solutions, and so on. The best solutions are carried over the next generation every time, in addition, random mutations in the offspring are implemented.

In the genetic algorithm, every solution is formed by values of the four fiber parameters (r_{core}, NA, Δ and Δ_p), and an associated fitness value. The fitness value is obtained from a fitness function defined as $\Delta k_T = |\Delta k_A| + |\Delta k_B| + |\Delta k_C|$, where Δk_I is the phase mismatch for process $I = A, B, C$. When the algorithm includes more than one pump wavelength at the same time, the value for the fitness function is written as $\Delta k_T = \sum_i |\Delta k_{Ai}| + |\Delta k_{Bi}| + |\Delta k_{Ci}|$, where Δk_{Ii} is the phase mismatch for process $I = A, B, C$ for the pump wavelength i. The algorithm is repeated looking for the condition $\Delta k_T = 0$ on one hand, and on the other hand the matching with the experimental maxima. The values of the parameters that generate numerical curves such that a triple

	p1	p2	s($\lambda > \lambda_p$)	i($\lambda < \lambda_p$)
peaks A	**01x**	**11ex**	**01y**	**11ey**
peaks B	**01x**	**11ox**	**01y**	**11oy**
peaks C	**01x**	**01x**	**01y**	**01y**
	11ex	11ex	01y	01y
	11ox	11ox	01y	01y
others	01x	01x	11ey	11ey
	01x	01x	11oy	11oy
	01x	11ex	11ey	01y
	01x	11ox	11oy	01y
	11ex	11ex	11ey	11ey
	11ex	11ex	11oy	11oy
	11ex	11ox	11ey	11oy
	11ex	11ox	11oy	11ey
	11ox	11ox	11ey	11ey
	11ox	11ox	11oy	11oy

Table 5.2: List of cross-polarized $xx-yy$ SFWM processes which conserve orbital angular momentum and parity in *HB800C* optical fiber.

intersection with the experimental peaks is obtained, are considered as candidates to explain the fiber. The algorithm leads to a set of solutions for the fiber parameters (r_{core}, NA, Δ, and Δ_p), all of them involving the processes shown in bold typeface in table 5.2. In the table 5.2 are listed the 15 possible processes viable in the *HB800C* optical fiber. The processes are grouped according to which are compatible with the pair of peaks from $A/B/C$ processes as well as those which are not compatible with any of these pair of peaks.

The numerical analysis of the SFWM processes suggest that there are different families of parameters that are compatible with the experimental measurements, specifically a continuum of solutions. Indicating what may be regarded as a continuum of equivalent fibers all of which would yield a similar SFWM behavior. Among the family of solutions found, there are two which are of particular interest. The first one, related with values

of the parameters $r_{core} = 1.45\mu m$, $NA = 0.20$, $\Delta = 2.38 \times 10^{-4}$ and $\Delta_p = 4.57 \times 10^{-4}$ is the one that minimizes Δk_T. The second one, related with values of the parameters $r_{core} = 1.742\mu m$, $NA = 0.167$, $\Delta = 2.37 \times 10^{-4}$ and $\Delta_p = 4.41 \times 10^{-4}$ is compatible with the values of the parameters provided by the manufacturer, with exception of Δ_p. Further information about the continuum of solutions is present in [37].

In figure 5.15 the numerical phasematching curves are displayed together with the experimental points, the two solutions identified in the previous paragraph yield essentially the same phase-matching characteristics, and there is agreement between theory and experiment. From figure 5.9 it is possible to note that the experimental peaks have different heights, that characteristic can be explained in terms of the process efficiency. The process efficiency depends on i) the overlap of the four transverse modes, and ii) the amount of power coupled in each pump mode. Such conditions can explain the higher count rate of process C with respect to A and B processes. By preparing the pump modes and its relative power, it is possible to control the efficiency SFWM process. In addition of the difference between the peaks height for every pump wavelength, the smallest peaks (A and B) show a decrease in the count rate when the pump wavelength increases, such behavior could be explained by the fact that the pump wavelength approaches the cut-off wavelength for the LP_{11}^{ex} and LP_{11}^{ox} modes, which take part as pumps for A and B processes, see table 5.2.

The numerical analysis allowed the SFWM processes identification, but it can be also used inversely as a technique to characterize the values of the fiber parameters. By considering the SFWM experimental measurements it is possible to calculate the values of the parameters that best fit the experimental behaviour.

Now the SFWM processes have been identified, it is possible to generate the joint

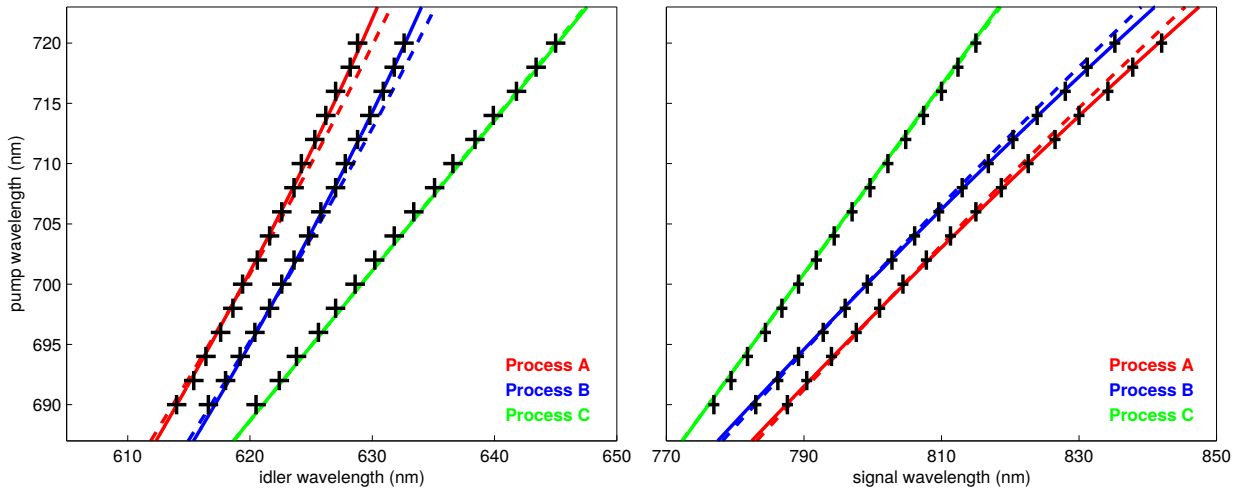

Figure 5.15: Comparison between experimental points and curves obtained from simulations for *HB800C* optical fiber.

spectral amplitude to characterize the photon pair correlation. Considering the values of the parameters $r_{core} = 1.742\mu m$, $NA = 0.167$, $\Delta = 2.37 \times 10^{-4}$ and $\Delta_p = 4.41 \times 10^{-4}$, a fiber length of $L = 14.5cm$ and a pump bandwidth of $\Delta\lambda_{pump} = 0.52nm$ the JSA (then the JSI) was calculated using equation (3.17), in addition the Schmidt number was obtained from the calculated JSA. The figure 5.16 shows the JSI simulations performed, it can be seen that the three processes are nearly-factorable, in agreement with the experimental measurements.

In the next part, the ability to produce entangled photon pairs in the *HB800C* optical fiber will be discussed. The number of SFWM processes in the fiber could grow if the number of supported modes increases, two possibilities makes that possible: i) decrease the pump wavelength (and therefore the generated photons wavelength), or ii) increase the core size (preserving the NA, Δ and Δ_p values). For instance, if the LP_{11}^{ey} and LP_{11}^{oy} modes were supported in the *HB800C* optical fiber for the higher wavelength

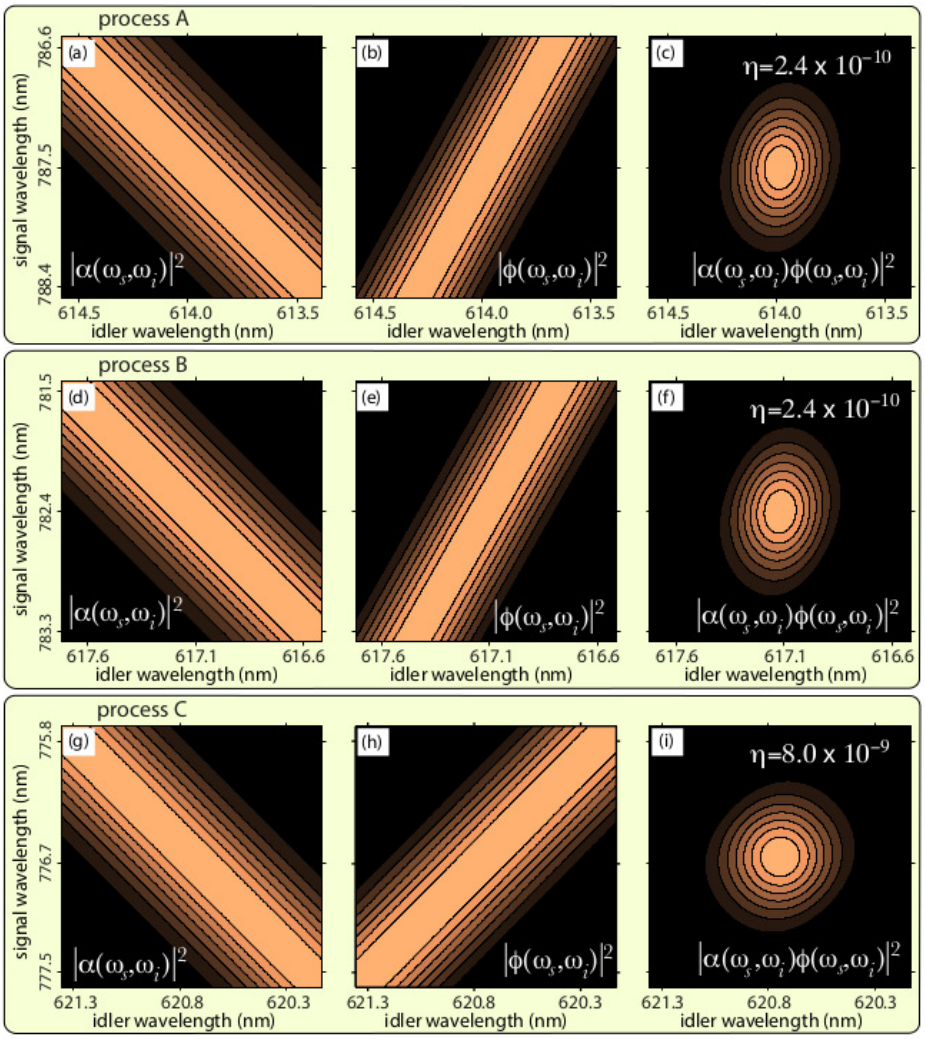

Figure 5.16: Numerical JSI for processes A, B, and C for *HB800C* optical fiber. First column shows $|\alpha(\nu_s, \nu_i)|^2$. Second column shows $|\phi(\nu_s, \nu_i)|^2$. Third column shows $|\alpha(\nu_s, \nu_i)\ \phi(\nu_s, \nu_i)|^2$.

process	p_1	p_2	i ($\lambda < \lambda_p$)	s ($\lambda > \lambda_p$)
a	11ox	11ox	11ey	11ey
b	01x	01x	01y	01y
c	01x	11ex	01y	11ey
d	01x	11ox	11oy	01y
e	01x	11ox	01y	11oy
f	11ex	11ox	11oy	11ey
g	01x	11ex	11ey	01y
h	11ex	11ex	11ey	11ey
i	11ox	11ox	11oy	11oy
j	11ex	11ox	11ey	11oy

Table 5.3: Mode combination for the SFWM processes in the *HB800G* optical fiber.

photon ($\lambda > \lambda_p$) as is the case for the lower wavelength photon ($\lambda < \lambda_p$), the number of processes would be 10 instead of 3. In the table 5.3 are listed the new 10 possible processes in the *HB800C* optical fiber.

In the figure 5.17 the JSI for the 10 process mentioned is shown. The JSI was calculated by considering the same values of the parameters of *HB800C* fiber, but a pump centered at $\lambda_p = 620nm$ with bandwidth $\Delta\lambda = 0.35nm$, and a fiber length of $L = 12cm$ were contemplated. From the figure 5.17 it can be seen that almost each processes is nearly-factorable, except the process (a), which is spectrally distant from the others. The processes with higher count rates are (b), (h) and (i), because the well overlap between the four transverse modes in each process. The processes (h) and (i) deserve special attention because both processes exhibit the same spectral behaviour and because the transverse modes of the generated photons are such that can be employed to prepare a hybrid entangled state as $r|LP_{11}^{ey}\rangle_{\lambda_s}|LP_{11}^{ey}\rangle_{\lambda_i} + s|LP_{11}^{oy}\rangle_{\lambda_s}|LP_{11}^{oy}\rangle_{\lambda_i}$ where $\lambda_s \approx 679.7nm$ and $\lambda_i \approx 570.0nm$. In the case of $|r| = |s| = 1/\sqrt{2}$ would be a Bell like state with spatial entanglement. Unfortunately this configuration is outside of Ti:sapphire laser capabilities.

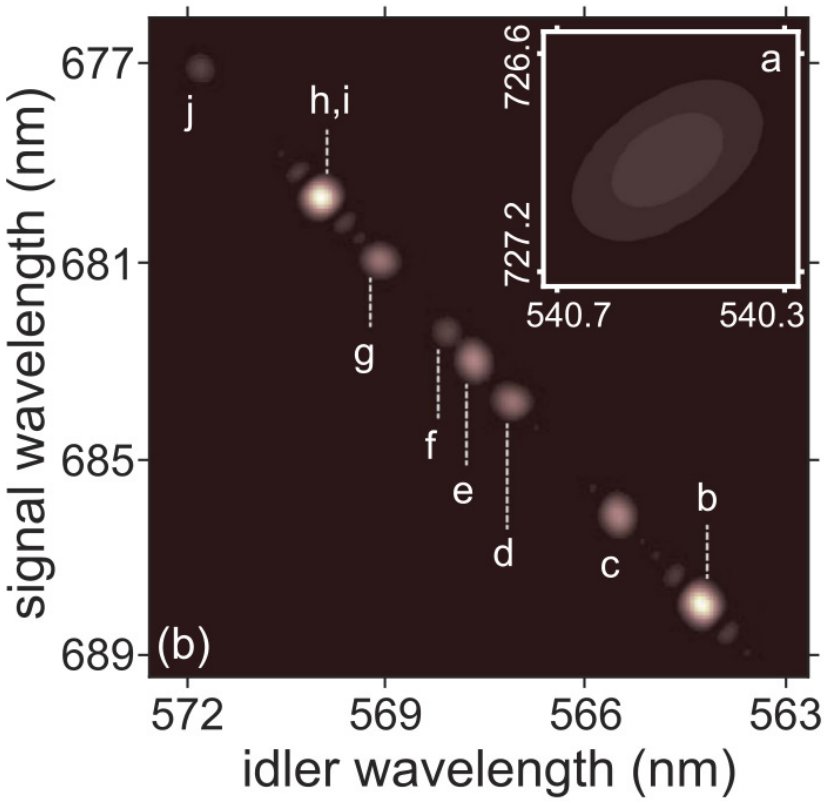

Figure 5.17: Numerical JSI for *HB800C* considering a pump of $620nm$.

Chapter 6

Tuning the Spatial Properties of the Photon Pair Source via a Mode Selective Photonic Lantern

Along the next lines will be described the transverse structure manipulation of heralded single photons generated in birefringent optical fiber. In order to perform the manipulation a device called mode selective photonic lantern (MSPL) was employed. In addition a scheme based on the use of a intensified CCD camera (ICCD) to record the transverse structure was developed.

The photonic lantern with which the photon transverse structure was modified has six terminals that correspond to the LP_{01}, LP_{11a}, LP_{11b}, LP_{21a}, LP_{21b} and LP_{02} modes. It is important to mention that the photonic lantern employed was fabricated by the Microstructured Fibers and Devices, CREOL group. That photonic lantern was designed to work in the wavelengths range where the photons are produced.

6.0.5 Exciting the Photonic Lantern Terminals

In figure 6.1 is shown the setup used in order to modify the transverse structure of single photons. The photon pair source is identical to the one described above employing a *HB800C* fiber. The lower wavelength photon arm was coupled into a multi-mode fiber (MMF2) using a $8mm$ aspheric lens and connected to the monochromator that is fitted to an photodiode (APD), this allowed to select a specific SFWM process among the three present. In order to simplify the measurements the process with the four waves in the fundamental mode LP_{01} was selected because the higher count rate. The higher wavelength photon arm was coupled and out-coupled into single-mode fiber (SMF) using two $8mm$ aspheric lenses, then was coupled to the mode selective photonic lantern (MSPL) with a $8mm$ aspheric lens, finally the output was imaged with the help of one $8mm$ aspheric lens on the ICCD (Andor iStar CCD 320) plane. In order to record the coincidences the photodiode signal was sent to a function generator (Stanford Research Systems DG535) to generate a TTL pulse ($5ns$ width and $2.5V$ height) whose signal was temporary controlled to balance the paths delay. The new signal produced by the function generator triggered the ICCD. The implementation of this technique allowed to reduce the acquisition time with respect to the previous rasterization technique.

To begin with the manipulation, only one terminal was select to be excited each time with the higher wavelength photon. The selected arm was coupled and out-coupled in the photonic lantern (MSPL) using two $8mm$ aspheric lenses. In figure 6.2 is shown the setup used.

In the figure 6.3 is shown the intensity pattern recorded by the ICCD when only one terminal is excited with the higher wavelength photon each time. When a particular terminal was excited only one LP_{lm} mode was obtained, in addition the excited mode corresponded to the associated terminal. The behaviour with the heralded photon and

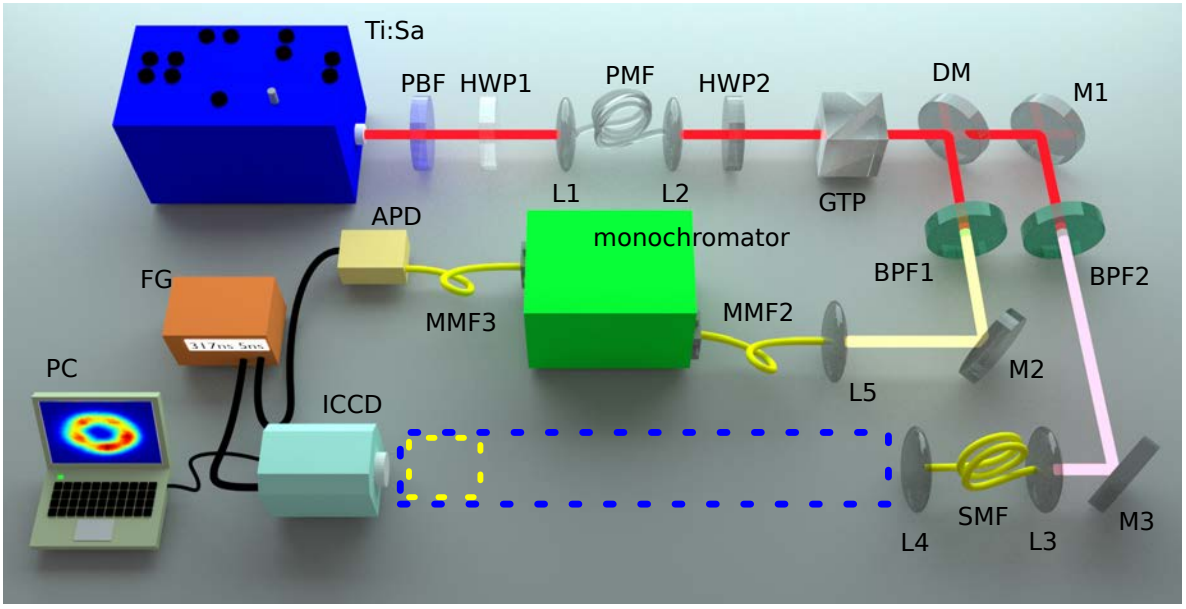

Figure 6.1: Setup used to modify and record the transverse structure of single photons using a photonic lantern.

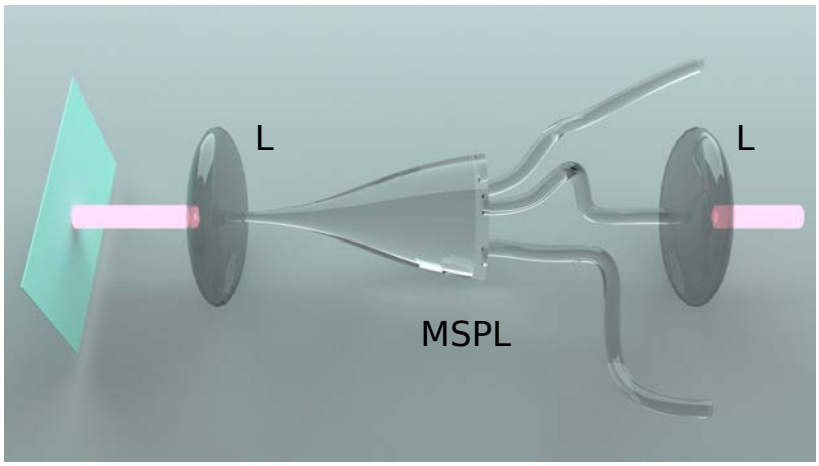

Figure 6.2: Scheme used to excite only one of the six terminals of the photonic lantern.

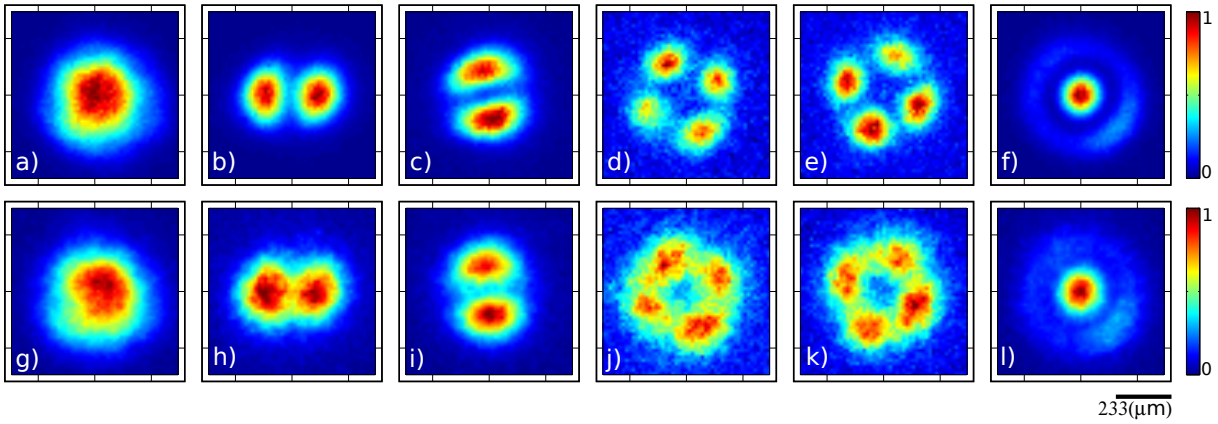

Figure 6.3: First row shows single counts for each photonic lantern terminal excited. Second row shows coincidence counts.

non heralded photon is analogous.

The next step in the manipulation was select two terminals to be excited at the same time with the higher wavelength photon. The excitation of the two terminals can be made coherently or incoherently. In the incoherent case the path-length difference is larger than the coherence length of the two photons. Meanwhile, in the coherent case the path-length difference is enough less than the coherence length permitting interference between them.

In the figure 6.4 is shown the setup to excite incoherently two terminals. The arm corresponding to higher wavelength photon was split using a half wave plate (Thorlabs AHWP05M-600) and a polarized beam splitter (Thorlabs PBS052), the polarization was then adjusted with a half wave plate (Thorlabs AHWP05M-600). Both paths were coupled using $8mm$ aspheric lenses in different photonic lantern terminals, the terminals corresponding to LP_{21a} and LP_{21b} modes were selected. Finally, the light was out-coupled with another $8mm$ aspheric lens. Data were taken for different values of the power ratio between the two arms and keeping the path length difference constant.

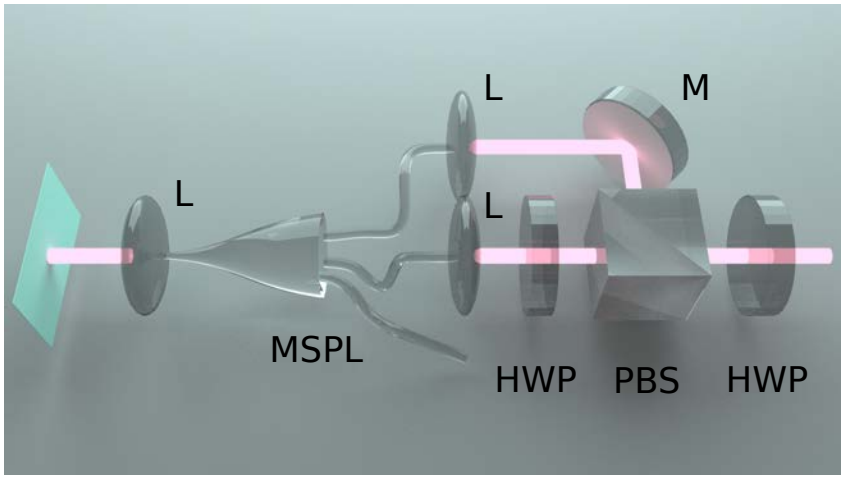

Figure 6.4: Scheme used to excite two photonic lantern terminals incoherently.

The figure 6.5 shows the result of excite incoherently two photonic lantern terminals. In the incoherent sum case it was possible to obtain an output ranging from LP_{21a} to LP_{21b}, as a function of the power ratio between the two terminals. The figure 6.5 presents the results of some specific splitting values of the pump power (numerical and experimental).

In figure 6.6 is illustrated the setup to excite coherently two terminals. The arm corresponding to higher wavelength photon was split using a half wave plate and a polarized beam splitter, the path length difference was regulated using a retro reflector (Thorlabs HR1015-P01) controlled with a motorized stage (New Focus 9062-X-P-M). The polarization was then adjusted with another half wave plate, both paths were coupled using $8mm$ aspheric lenses in different photonic lantern terminals, the terminals corresponding to LP_{21a} and LP_{21b} modes were selected. Finally the light was out-coupled with another $8mm$ aspheric lens. In this case data were taken for different values of the path length difference between both arms and keeping the power ratio constant.

The figure 6.7 shows the behavior of excite coherently two photonic lantern terminals.

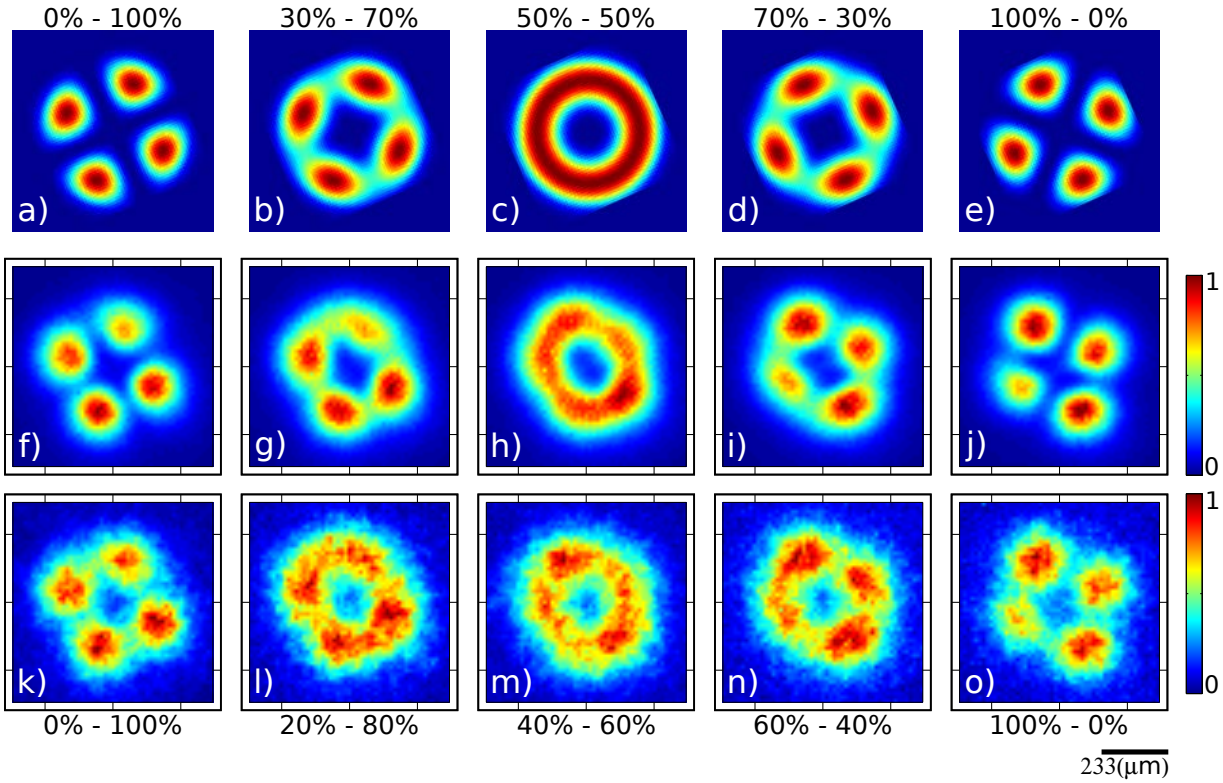

Figure 6.5: Incoherent sum of LP_{21a} and LP_{21b} modes. First row shows numerical intensity. Second row shows single counts. Third row shows coincidence counts.

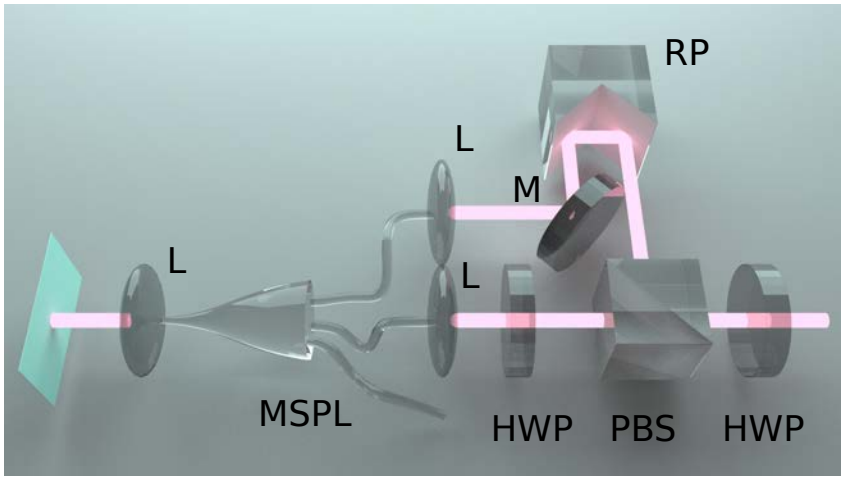

Figure 6.6: Scheme used to excite two photonic lantern terminals coherently.

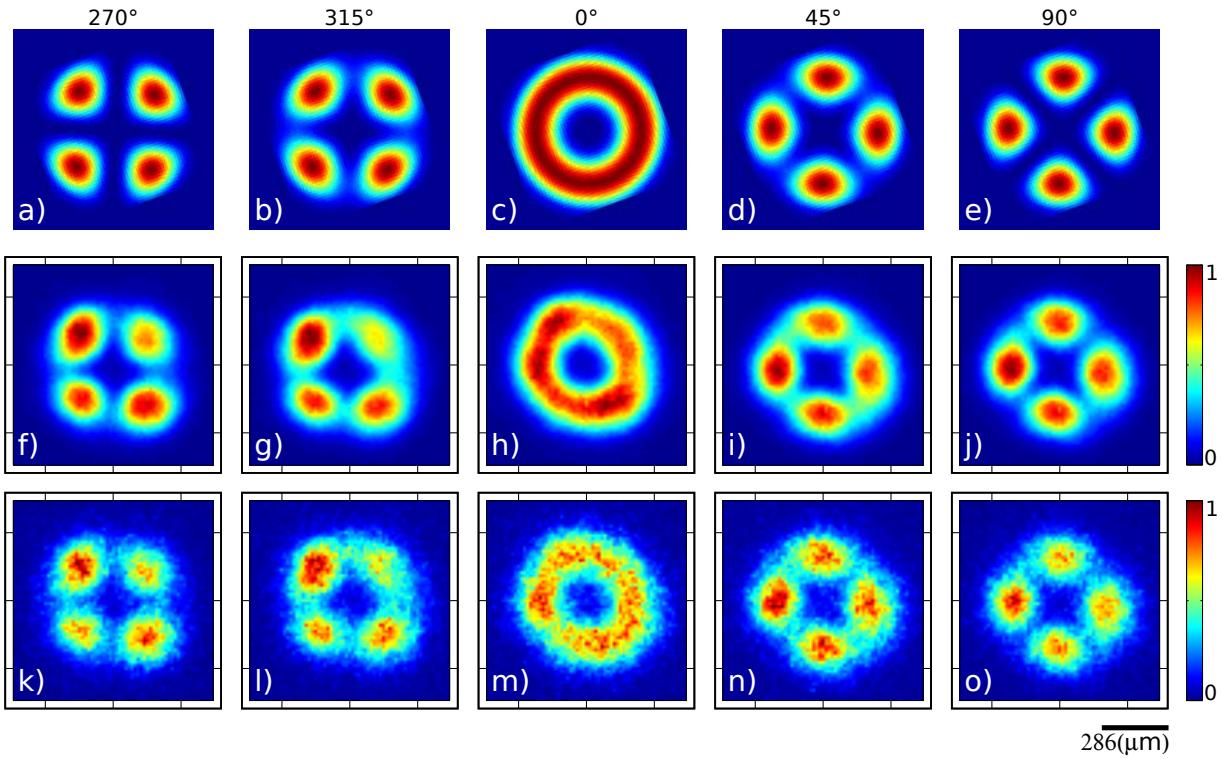

Figure 6.7: Coherent sum of LP_{21a} and LP_{21b} modes. First row shows numerical intensity. Second row shows single counts. Third row shows coincidence counts.

In the case of the coherent sum it was possible to obtain an output ranging from LP_{21a} to LP_{21b} by changing the path length difference (phase) between the two terminals. The figure 6.7 shows the results for specific phase values.

6.0.6 Discriminating the Photonic Lantern Behaviour

When the coherent and incoherent sums were considered, the intensity pattern behavior is very similar. But the experiment performed is totally different: variable power ratio in the incoherent case against variable phase in the coherent case. In order to discriminate between the incoherent and coherent case it becomes necessary employ a phase sensitive

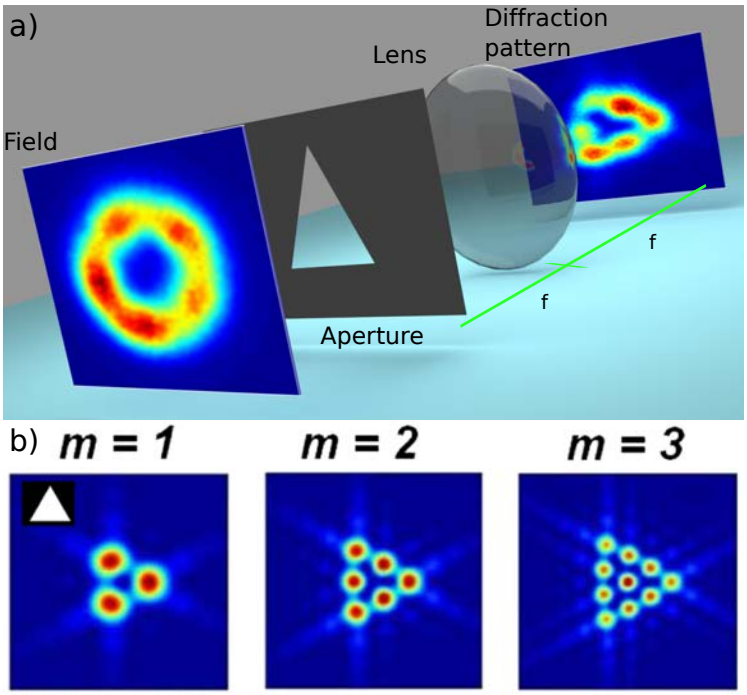

Figure 6.8: a) Far field diffraction technique. b) Far field diffraction pattern for beams with different topological charge.

technique. A technique based on far field diffraction through a triangular aperture [43] was used, such technique reveals quantitative information about the topological charge of the photons, i.e orbital angular momentum. When a triangular pattern appears in the Fourier plane the topological charge is equal to the number of lobes on one side minus one as $tp = l - 1$.

In figure 6.9 the experimental implementation to discriminate coherent and incoherent sum, is shown. After the two different photonic lantern terminals were excited using $8mm$ aspheric lenses, the beam was out-coupled and imaged in a specific plane using another $8mm$ aspheric lens, in the image plane was placed a triangular aperture (National Aperture Inc. 214-0256) of $250\mu m$ side. A f-f arrangement using a $10cm$ lens (Thorlabs LA1509-B) was mounted to obtain the far field diffraction pattern. The

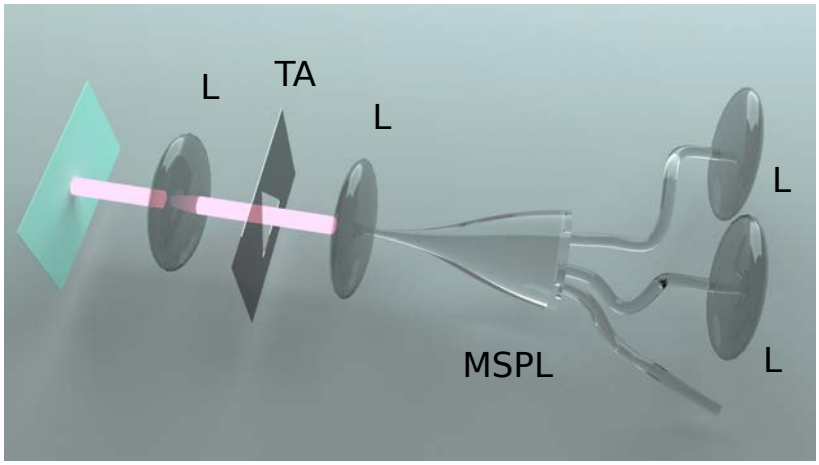

Figure 6.9: Scheme used to determine the coherent or incoherent excitation of the two photonic lantern terminals.

chosen configurations to apply the diffraction technique were those where a doughnut shaped intensity was observed such as figure 6.5c) and figure 6.7c).

The figure 6.10 shows the far field diffraction pattern for coherent and incoherent cases. The far field diffraction patterns for the coherent and incoherent cases are very different. In the incoherent case the pattern is hexagonal, while in the coherent case is triangular. It is important to note from the coherent case, that the photonic lantern can be exploited to prepare single photons with explicit orbital angular momentum.

6.0.7 Photonic Lantern Discussion

The spatial measurements shown in the figures 6.3, 6.5, and 6.7 prove that the mode selective photonic lantern can be used to deterministically modify the transverse structure of single photons. The number of single-modes accessible in the MSPL is the same to the number of terminals, see figure 6.3, this number is fixed for a given device, but in principle it can be scaled. When more than one terminal is considered

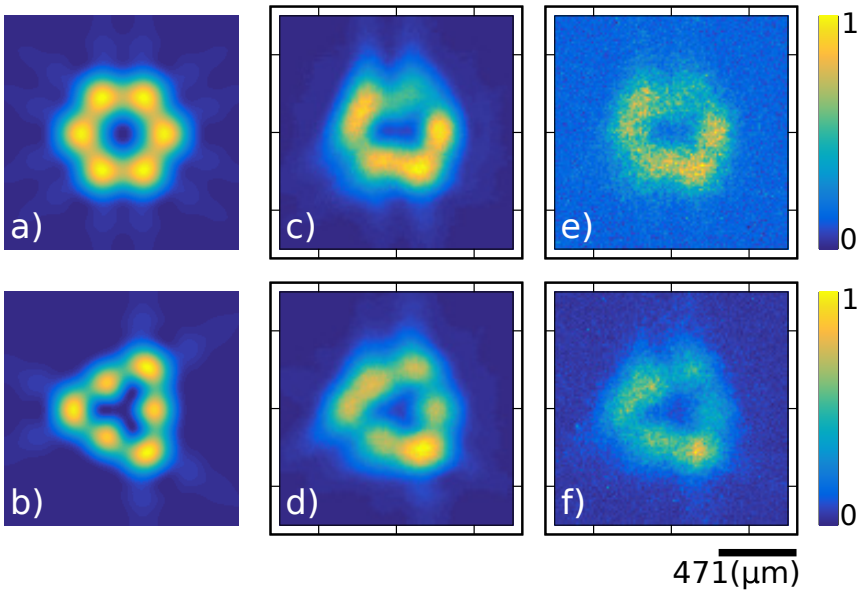

Figure 6.10: Far field diffraction. First row shows numerical, single counts and coincidence counts for incoherent sum. Second row shows numerical, single counts and coincidence counts for coherent sum.

the excitation can be: i) coherent (see figure 6.7), ii) incoherent (see figure 6.5) or iii) partial. In the coherent case it is possible write an expression for the total field as $E = \sum_j \alpha_j \ \exp(i\phi_j)\ E(LP_{lm,j})$. While, in the incoherent case it is not possible to write the total field, only the intensity is known $I = \sum_j \beta_j \ I(LP_{lm,j})$.

The excitation of terminals with the same topological charge is of special interest, this condition is fulfilled with the pairs LP_{11a} - LP_{11b} and LP_{21a} - LP_{21b} for example. For the coherent and incoherent excitations there are specific values of α, and ϕ, and β respectively, that generate the same kind of intensity patterns for each case, see figure 6.7 and figure 6.5. The discrimination between both cases is possible using a phase sensitive technique, as the far field diffraction through a triangular aperture figure 6.10. Furthermore, considering the coherent sum case with same power ratio in both terminals, the total field can be written as

$$E = \alpha \left[E(LP_{lm,a}) + \exp\left(i\phi\right)\, E(LP_{lm,b}) \right], \tag{6.1}$$

where l and m are identical for both fields, and ϕ is a relative phase between the fields. The terminal associated with LP_{lma} produces a transverse field profile proportional to $\cos(l\phi)$, meanwhile the terminal associated with LP_{lmb} produces a transverse field profile proportional to $\sin(l\phi)$, these modes are composed of superpositions of underlying vortices $exp(il)$ and $exp(-il)$, one way to access the implied orbital angular momentum (OAM) is to construct superpositions of both as

$$\begin{aligned} LP^{*}_{lm} &= \frac{1}{\sqrt{2}}(LP_{lma} + LP_{lmb}), \\ LP^{*}_{-lm} &= \frac{1}{\sqrt{2}}(LP_{lma} - LP_{lmb}). \end{aligned} \tag{6.2}$$

Due the photonic lantern principle, which makes possible generate fields with a structure described by equation (6.1), it is also possible to use it in the opposite way: for analyze a field composed of LP modes, which will imply a sorting of the modes and the knowledge of the relative phase between them. The aforementioned characteristic could be useful for entanglement analysis in the spatial degree of freedom, as an analogy to the better known polarization case $Pol = H + \exp(i\varphi)V$.

Chapter 7

Conclusions

In this work has been studied two photon pair sources based on birefringent optical fiber, via Spontaneous Four Wave Mixing (SFWM) process. The configuration of all the SFWM processes is co-propagating, each one of the four participating waves travel in the same direction in the optical fiber. In addition, the SFWM processes were cross-polarized, the generated photons are orthogonal to the pump photons. Both sources were selected to allow higher order modes can propagate in the optical fibers, enabling several SFWM processes occur simultaneously.

Furthermore, the use of a mode converter based in optical fiber, the mode selective photonic lantern (MSPL), was proved to modify the transverse structure of single photons from LP_{01} mode to another LP_{lm} modes. In addition, it is possible to prepare a coherent combinations of LP modes to obtain single photons with explicit orbital angular momentum (OAM).

The first source based on $HB800G$ optical fiber exhibits four different processes, which were identified by spectral characterization. The description of this source was

based on a modified step index model, however the stress applying parts (SAPs) in the fiber are very near to the core and it is not clear whether the mode can overlapping with them or not. The analysis of the source used a numerical technique to explain the experimental peaks, numerical phasematching curves were generated looking for the intersection with the experimental peaks. The technique considered the fiber parameters: core radius, numerical aperture and birefringence.

While, for the second source based on $HB800C$ optical fiber, it shows three simultaneous processes. Again, the processes were identified by spectral characterization, in addition, the spatial structure of the generated photons, and the joint spectral intensity were also measured. For this optical fiber the SAPs are sufficiently separated from the core to avoid overlapping with them. The description of this source included a novel element: the parity birefringence Δ_p, without which it is not possible to explain the SFWM processes obtained. Numerical phasematching curves were generated employing a genetic algorithm, these curves were generated searching the intersection with the experimental peaks. The technique considered the fiber parameters: core radius, numerical aperture, birefringence and parity birefringence. For the $HB800C$ optical fiber source it has also been shown the ability to tune the spectral behavior of the generated photons by manipulating the pump wavelength within the range $690nm$ to $720nm$. The design of the source was chosen to show nearly uncorrelated spectral photon pairs in each process supported in the fiber. Moreover, the source is capable of hybrid spectrum-spatial entanglement, unfortunately the specific conditions for the pump are out of the possibilities of the work laser.

As a general characteristic, the photon pairs generated in both sources are spectrally non degenerated, making possible to discriminate the different SFWM processes by

spectral filtering. This characteristic is convenient in order to select groups of process to obtain specific photon states. Among the main advantages of fiber based sources are the direct compatibility with fiber networks used for telecommunications, as well as the exact description of the transverse structure of the generated photons. Also, the sources based on optical fiber are very promising as building blocks for quantum optics applications due to the flexibility in the photon pair state design.

Furthermore, the numerical analysis of the experimental data enabled identify the SFWM processes in the fiber, but it can be used inversely to obtain values for the fiber parameters, in such a way that the numerical analysis is an alternative technique to characterize the fiber.

The use of a MSPL allowed the manipulation of the transverse structure of single photons, which offers the opportunity to increase controllably its accessible degrees of freedom. The single photons can be prepared using the MSPL in well defined LP modes as well as in a combination of them. Moreover, the combination can be coherent and incoherent, and it is possible to discriminate between both kind of excitation using a phase sensitive technique. Then, single photons with explicit orbital angular momentum can be prepared using the coherent excitation of the MSPL. It is expected the use of this kind of devices to analyze beams conformed by the coherent combination of different LP modes, in a clear analogy to the polarization case.

Chapter 8

Conclusiones

En este trabajo han sido estudiadas dos fuentes de parejas de fotones basadas en fibra óptica birrefringente, a través del proceso de mezcla espontánea de cuatro ondas (SFWM). La configuración de todos los procesos SFWM es co-propagante, cada una de las cuatro ondas participantes viaja en la misma dirección en la fibra óptica. Además los procesos de SFWM fueron contra-polarizados, los fotones generados son ortogonales a los fotones de bombeo. Ambas fuentes fueron seleccionadas para permitir que modos de orden superior puedan propagarse en las fibras ópticas, permitiendo que varios procesos de SFWM ocurran simultáneamente.

Además, el uso de un conversor de modos basado en fibra óptica, la linterna fotónica (MSPL), fue provado para modificar la estructura transversal de fotones individuales del modo LP_{01} a otros modos LP_{lm}. También, es posible preparar una combinación coherente de modos LP para obtener fotones individuales con momento angular orbital (OAM) explícito.

La primera fuente basada en fibra $HB800G$ exhibe cuatro diferentes procesos, los

cuales fueron identificados por caracterización espectral. La descripción de esta fuente fue basada en un modelo modificado de fibra escalonada, sin embargo las partes que aplican estrés (SAPs) en la fibra se encuentran muy cerca del núcleo y no es claro si el modo puede traslaparse con ellas o no. El análisis de la fuente usó una técnica numérica para explicar los picos experimentales, curvas numéricas fueron generadas buscando la intersección con los picos experimentales. La técnica consideró los parámetros de fibra: radio del núcleo, apertura numérica y birrefringencia.

Mientrás, para la segunda fuente basada en fibra óptica $HB800C$, esta muestra tres procesos simultáneos. De nuevo los procesos fueron identificados por caracterización espectral, además, la estructura espacial de los fotones generados, y la intensidad espectral conjunta fueron también medidos. Para esta fibra óptica los SAPs están suficientemente separados del núcleo para evitar el traslape con ellos. La descripción de esta fuente incluyó un elemento novedoso: la birrefringencia de paridad Δ_p, sin el cual no es posible explicar los procesos de SFWM obtenidos. Curvas numéricas fueron generadas empleando un algoritmo genético, esas curvas fueron generadas buscando la intersección con los picos experimentales. La técnica considera los parámetros de fibra: radio del núcleo, apertura numérica, birrefringencia y birrefringencia de paridad. Para la fuente en la fibra $HB800C$ también se ha mostrado la capacidad de sintonizar el comportamiento espectral de los fotones generados manipulando la longitud de onda del bombeo dentro del intervalo $690nm$ a $720nm$. El diseño de la fuente fue seleccionado para mostrar casi no-correlación espectral en cada proceso soportado en la fibra. Más aún, la fuente es capaz de enredamiento híbrido espectro-espacial, desafortunadamente las condiciones específicas para el bombeo están fuera de las posibilidades del láser de trabajo.

Como una característica general, los parejas de fotones generadas en ambas fuentes

son no degeneradas espectralmente, haciendo posible discriminar los diferentes procesos SFWM mediante filtraje espectral. Esta característica es conveniente para seleccionar grupos de procesos para obtener estados de fotones específicos. Entre las principales ventajas de las fuentes basadas en fibra están la compatibilidad directa con redes de fibra usadas para telecomunicaciones, así como la descripción exacta de la estructura transversal de los fotones generados. También, las fuentes basadas en fibra óptica son muy prometedoras para aplicaciones de óptica cuántica debido a la flexibilidad en el diseño de la pareja de fotones.

También, el análisis numérico de los datos experimentales permitió identificar los procesos SFWM en la fibra, pero este puede ser usado al revés para obtener valores para los parámetros de la fibra, de tal manera que el análisis numérico es una técnica alternativa para caracterizar la fibra.

El uso de una MSPL permitió la manipulación de la estructura transversal de fotones individuales, lo cual ofrece la de incrementar controlablemente sus grados de libertad accesibles. Los fotones individuales pueden ser preparados usando la MSPL en modos LP bien definidos así como en una combinación de ellos. Además la combinación puede ser coherente e incoherente, y es posible discriminar entre ambos tipos de excitación usando una técnica sensible a la fase. Así, fotones individuales con momento angular explícito pueden ser preparados usando la MSPL. Se espera el uso de este tipo de dispositivo para analizar haces conformados por la combinación coherente de diferentes modos LP, en una clara analogía con el caso de la polarización.

Appendix A

Detector especifications

The APD has a dead-time of $80ns$ and dark counts in the order of 250 to 350 per second, presents a wavelength response curve which is shown in figure A.1

The monochromator grating with $1200l/mm$ presents a wavelength response curve that is shown in figure A.2

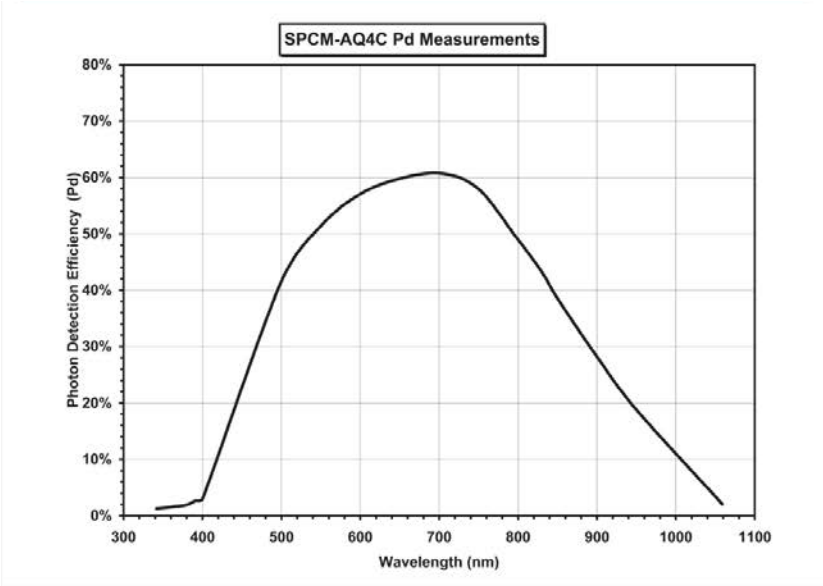

Figure A.1: Wavelength response curve for APD as provided by manufacturer.

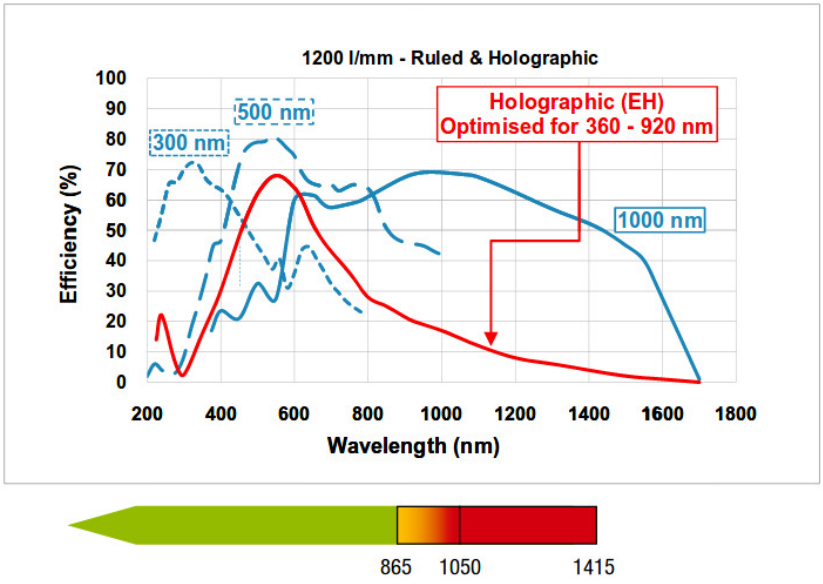

Figure A.2: Wavelength response curve for monochromator grating as provided by manufacturer.

Bibliography

[1] Shadbolt, P., Mathews, J. C. F., Laing, A. and O'Brien, J. L., *Testing foundations of quantum mechanics with photons*, Nat. Phys. **10**, 278286 (2014).

[2] Gisin, N. and Thew, R., *Quantum communication* Nat. Photon. **1** 165-71 (2007).

[3] Bennett, C. H., Bessette, F., Brassard, G., Salvail, L. and Smolin, J. *Experimental Quantum Cryptography*, J. Cryptology **5**, 3 (1992).

[4] Gisin, N., Ribordy, G., Tittel, W. and Zbinden, H. *Quantum cryptography*, Rev. Mod. Phys. **74**, 145 (2002).

[5] Ribordy, G., Gautier, J. D., Gisin, N., Guinnard, O. and Zbinden, H. *Fast and user-friendly quantum key distribution*, J. Mod. Opt. **47**, 517 (2000).

[6] S. Etcheverry, G. Cañas, E. S. Gómez, W. A. T. Nogueira, C. Saavedra, G. B. Xavier, and G. Lima, *Quantum key distribution session with 16-dimensional photonic states*, Sci. Rep. **3**, 02316 (2013).

[7] Bouwmeester, D., Pan, J. W., Mattle, K., Eibl, M., Weinfurter, H. and Zeilinger, A. *Experimental quantum teleportation*, Nature **390**, 575 (1997).

[8] Kok, P., Munro, W. J., Nemoto, K., Ralph, T. C., Dowling, J. P. and Milburn, G. J. *Linear optical quantum computing with photonic qubits*, Rev. Mod. Phys **79**, 797 (2007).

[9] O'Brien, J. L., Furusawa, A., and Vučković, J., *Photonic quantum technologies*, Nat. Photon. **3**, 687 (2009).

[10] Kwiat, P.G., Mattle, K., Weinfurter, H., and Zeilinger, A., *New high-intensity source of polarization-entangled photon pairs*, Phys. Rev. Lett. **75**, 4337-4341 (1995).

[11] Santori, C., Fattal, D., Vuckovic, J., Solomon, G. S. and Yamamoto, Y. *Single-photon generation with InAs quantum dots*, New J. Phys. **6**, 89 (2004).

[12] Sharping, J. E., Fiorentino, M., and Kumar, P. *Observation of twin-beam-type quantum correlation in optical fiber*, Opt. Lett. **26**, 367 (2001).

[13] A. Kuzmich, W. P. Bowen, A. D. Boozer, A. Boca, C. W. Chou, L.-M. Duan and H. J. Kimble, *Generation of nonclassical photon pairs for scalable quantum communication with atomic ensembles* Nature **423** 731-734 (2003).

[14] D. C. Burnham and D. L. Weinberg, *Observation of Simultaneity in Parametric Production of Optical Photon Pairs*, Phys. Rev. Lett. **25**, 84-87 (1970).

[15] Garay-Palmett, K., McGuinness, H. J., Cohen, O., Lundeen, J. S., Rangel-Rojo, R., U'Ren, A. B., Raymer, M. G., McKinstrie, C. J., Radic, S. and Walmsley, I. A. *Photon pair-state preparation with tailored spectral properties by spontaneous four-wave mixing in photonic-crystal fibers*, Opt. Express **15**, 14870 (2007).

[16] Smith, B. J., Mahou, P., Cohen, O., Lundeen, J. S. and Walmsley, I. A. *Photon pair generation in birefringent optical fibers*, Opt. Express **17**, 23589 (2009).

[17] Zhou, Q., Zhang, W., Cheng, J., Huang, Y. and Peng, J. *Polarization-entangled Bell states generation based on birefringence in high non linear microstructure fiber at* $1.5\mu m$, Opt. Lett. **34**, 2706 (2009).

[18] Soller, C., Smith, B. J., Walmsley, I. A. and Silberhorn, C. *High-performance single-photon generation with commercial-grade optical fiber*, Phys. Rev. A **83**, 031806 (2011).

[19] Meyer-Scott, E., Roy, V., Buorgoin, J. P., Higgins, B. L., Shalm, L. K. and Jennewein, T. *Generatig polarization-entangled photon pairs using cross-spliced birefringent fibers*, Opt. Express **21**, 6205-6212 (2013).

[20] Fang, B., Cohen, O. and Lorenz, V. *Polarization-entangled photon-pair generation in commercial-grade polarization-maintaining fiber*, J. Opt. Soc. Am. B **31**, 277 (2014).

[21] Cruz-Delgado, D., Monroy-Ruz, J., Barragan-Diaz, A. M., Ortiz-Ricardo, E., Cruz-Ramirez, H., Ramirez-Alarcon, R., Garay-Palmett, K. and U'Ren, A. B. *Configurable spatio-temporal properties in a photon-pair source based on spontaneous four wave mixing with multiple transverse modes*, Opt. Lett. **39**, 3583-3586 (2014).

[22] Cruz-Delgado, D., Ramirez-Alarcon, R., Ortiz-Ricardo, E., Monroy-Ruz, J., Dominguez-Serna, F., Cruz-Ramirez, H., Garay-Palmett, K. and U'Ren, A. B. *Fiber-based photon-pair source capable of hybrid entanglement*

in frequency and transverse mode, controllably scalable to higher dimensions, Sci. Rep. **6**, 27377 (2016).

[23] Grier, D. G., *A revolution in optical manipulation*, Nature **424**, 810-816 (2003).

[24] Beijersbergen, M. W., Coerwinkel, R. P. C., Kristensen, M. and Woerdman, J. P., *Helical-wavefront laser beams produced with a spiral phaseplate* Opt. Commun. **112** 321-327 (1994).

[25] Y. Kang, J. Ko, S. M. Lee, S. -K. Choi, B. Y. Kim, and H. Park, *Measurement of the Entanglement between Photonic Spatial Modes in Optical Fibers* Phys. Rev. Lett. **109** 020502 (2012).

[26] Bharadwaj, D., Thyagarajan, K., Jachura, M., Karpinski, M., and Banaszek, K., *Scheme for on-chip verification of transverse mode entanglement using the electro-optic effect*, Opt. Express **23**, 33087-33098 (2015).

[27] Z. Bouchal, J. Wagner and M. Chlup, *Self-reconstruction of a distorted non-diffracting beam* Opt. Commun. **151** 207-211 (1998).

[28] H. He, M. E. J. Friese, N. R. Heckenberg and H. Rubinsztein-Dunlop, *Direct Observation of Transfer of Angular Momentum to Absorptive Particles from a Laser Beam with a Phase Singularity* Phys. Rev. Lett. **75** 826-829 (1995).

[29] J. Wang, J. -Y. Yang, I. M. Fazal, N. Ahmed, Y. Yan, H. Huang, Y. Ren, Y. Yue, S. Dolinar, M. Tur and A. E. Willner, *Terabit free-space data transmission employing orbital angular momentum multiplexing* Nat. Photon. **6** 488-496 (2012).

[30] Cruz-Delgado, D., Alvarado-Zacarias, J. C., Antonio-Lopez, E. R., Cruz-Ramirez, H., Leon-Saval, S. G., Amezcua-Correa, R. and U'Ren, A. B. *Deterministic transverse mode conversion at the single-photon level*, CLEO: Science and Innovations, STh1K. 3 (2017).

[31] S. G. Leon-Saval, A. Argyros, and J. Bland-Hawthorn, *Photonic Lanterns: a study of light propagation in multimode to single-mode converters*, Opt. Express **18**, 8430-8439 (2010).

[32] S. G. Leon-Saval, N. K. Fontaine, J. R. Salazar-Gil, B. Ercan, R. Ryf, and J. Bland-Hawthorn, *Mode-selective photonic lanterns for space-division multiplexing*, Opt. Express **22**, 1036 (2014).

[33] Agrawal, G. P., *Non Linear Fiber Optics* Academic Press, California, USA, Third Edition, 2001.

[34] Yariv, A. and Yeh, P., *Photonics*, Oxford University Press, New York, USA, Sixth Edition, 2007.

[35] Loudon, R., *Quantum Theory of Light*, Oxford University Press, Oxford, UK, 1992.

[36] Sakurai, J. J., *Modern Quantum Mechanics*, Addison-Wesley Publishing Company Inc., New York, USA, Revised Edition, 1994.

[37] Garay-Palmett, K., Cruz-Delgado, D., Dominguez-Serna, F., Ortiz-Ricardo, E., Monroy-Ruz, J., Cruz-Ramirez, H., Ramirez-Alarcon, R. and U'Ren, A. B. *Photon-pair generation by intermodal spontaneous four-wave mixing in birefringent, weakly guiding optical fibers*, Phys. Rev. A **93**, 033810 (2016)

[38] Grice, W. P. and Wamsley, I. A. *Spectral information and distinguishability in type-II down-conversion with a broadband pump*, Phys. Rev. A **56**, 1627-1634 (1997).

[39] Mosley, P. J., Lundeen, L. S., Smith, B. J., and Wamsley, I. A. *Conditional preparation of single photons using parametric downconversion: a recipe for purity*, New J. Phys. **10**, 093011 (2008).

[40] Law, C. K., Wamsley, I. A. and Eberly, J. H. *Continuous Frequency Entanglement: Effective Finite Hilbert Space and Entropy Control*, Phys. Rev. Lett. **84**, 5304 (2000).

[41] J. Montoya, C. Aleshire, C. Hwang, N. K. Fontaine, A. Velzquez-Bentez, D. H. Martz, T.Y. Fan, and D. Ripin, *Photonic lantern adaptive spatial mode control in LMA fiber amplifiers*, Opt. Express **24**, 3405 (2016).

[42] A. M. Velazquez-Benitez, J. C. Alvarado, G. Lopez-Galmiche, J. E. Antonio-Lopez, J. Hernndez-Cordero, J. Sanchez-Mondragon, P. Sillard, C. M. Okonkwo, and R. Amezcua-Correa, *Six mode selective fiber optic spatial multiplexer*, Opt. Lett. **40**, 1663-1666 (2015).

[43] J. M. Hickmann, E. J. S. Fonseca, W. C. Soares, S. Chávez-Cerda, *Unveiling a Truncated Optical Lattice Associated with a Triangular Aperture Using Light's Orbital Angular Momentum*, Phys. Rev. Lett. **105**, 053904 (2010).

[44] Mandel, L. and Wolf, E., *Optical Coherence and Quantum Optics*, Cambridge University Press, 1995.

[45] Boyd, R. W. *Non Linear Optics*, Academic Press, New York, USA, Second Edition, 2003.

[46] Shalm *et. al.*, *Strong Loophole-Free Test of Local Realism*, Phys. Rev. Lett. **115**, 250402 (2015).

[47] Bharadwaj, D., Thyagarajan, K., Karpinski, M., and Banaszek, K., *Generation of higher-dimensional modal entanglement using a three-waveguide directional coupler*, Phys. Rev. A **91**, 033824 (2015).

[48] R. Fickler, M. Krenn, R. Lapkiewicz, S. Ramelow, and A. Zeilinger, *Real-Time Imaging of Quantum Entanglement*, Sci. Rep. **3**, 1914 (2013).

[49] H. Di Lorenzo Pires, C. H. Monken, and M. P. van Exter, *Direct measurement of transverse-mode entanglement in two-photon states*, Phys. Rev. A **80**, 022307 (2009).

[50] D. S. Tasca, L. Rudnicki, R. S. Aspden, M. J. Padgett, P. H. Souto Ribeiro, and S. P. Walborn, *Testing for entanglement with periodic images*, arxiv

[51] G. Molina-Terriza, J. P. Torres, and Lluis Torner, *Twisted photons*, Nat. Phys. **3**, 305-310 (2007).

[52] H. Bechmann-Pasquinucci and W. Tittel, *Quantum cryptography using larger alphabets*, Phys. Rev. A **61**, 062308 (2000).

[53] M. Mirhosseini, O. S. Magaa-Loaiza, M. N O'Sullivan, B. Rodenburg, M. Malik, M. P. J. Lavery, M. J. Padgett, D. J. Gauthier and R. W Boyd, *High-dimensional quantum cryptography with twisted light*, New J. Phys. **17**, 033033 (2015).

[54] T. A. Birks, I. Gris-Snchez, S. Yerolatsitis, S. G. Leon-Saval and R. R. Thomson, *The photonic lantern*, Adv. Opt. Photon. **7**, 107 (2015).

[55] Giovannetti, V., Lloyd, S. and Maccone, L., *Advances in quantum metrology*, Nat. Photon. **5**, 222229 (2011).